Simulation of United States Mesoscale Convective Systems using GFDL's New High-Resolution General Circulation Model

WENHAO DONG,[a,b] MING ZHAO,[b] YI MING,[b] JOHN P. KRASTING,[b] AND V. RAMASWAMY[b]

[a] *Cooperative Programs for the Advancement of Earth System Science, University Corporation for Atmospheric Research, Boulder, Colorado*

[b] *NOAA/Geophysical Fluid Dynamics Laboratory, Princeton, New Jersey*

(Manuscript received 12 July 2022, in final form 9 May 2023, accepted 30 June 2023)

ABSTRACT: Accurate representation of mesoscale scale convective systems (MCSs) in climate models is of vital importance to understanding global energy, water cycles, and extreme weather. In this study, we evaluate the simulated MCS features over the United States from the newly developed GFDL global high-resolution (~50 km) AM4 model by comparing them with the observations during spring to early summer (April–June) and late summer (July–August). The results show that the spatial distribution and seasonality of occurrence and genesis frequency of MCSs are reasonably simulated over the central United States in both seasons. The model reliably reproduces the observed features of MCS duration, translation speed, and size over the central United States, as well as the favorable large-scale circulation pattern associated with MCS development over the central United States during spring and early summer. However, the model misrepresents the amplitude and the phase of the diurnal cycle of MCSs during both seasons. In addition, the spatial distribution of occurrence and genesis frequency of MCSs over the eastern United States is substantially overestimated, with larger biases in early spring and summer. Furthermore, while large-scale circulation patterns are reasonably simulated in spring and early summer, they are misrepresented in the model during summer. Finally, we examine MCS-related precipitation, finding that the model overestimates MCS-related precipitation during spring and early summer, but this bias is insufficient to explain the significant dry bias observed in total precipitation over the central United States. Nonetheless, the dry biases in MCS-associated precipitation during late summer likely contribute to the overall precipitation deficit in the model.

KEYWORDS: Atmosphere; North America; Mesoscale systems; Climate models

1. Introduction

Mesoscale convective systems (MCSs) play important roles in the hydrological cycle and global circulation through redistribution of heat, moisture, and momentum in the atmosphere (Hartmann et al. 1984; Fritsch et al. 1986; Houze 1989). They come into existence when isolated convective events aggregate and grow upscale into large clusters or even superclusters by forming mesoscale circulations (Mapes and Houze 1993; Houze 2004, 2018). Consequently, MCSs are characterized by distinct structures from scattered or isolated convection, consisting of active convective towers and expansive stratiform regions. Their sizes can reach several hundreds of kilometers with a lifetime ranging from a few hours to a few days (Houze 2004). The combination of convective and stratiform precipitation associated with MCSs is responsible for more than 50% of the total tropical rainfall (Nesbitt et al. 2006; Yuan and Houze 2010; Roca et al. 2014; Houze et al. 2015; Virts and Houze 2015; Tao and Chern 2017; Feng et al. 2021b). And the fraction can even reach up to 90% in the La Plata basin and more than 70% in the Sahel, the Congo basin, the central United States, and the west coast of Central America based on satellite observations (Nesbitt et al. 2006).

MCSs are often observed in heavily raining areas of the tropics and subtropics (Nesbitt et al. 2006; Yuan and Houze 2010; Dong et al. 2020, 2022) as well as midlatitude continents over prominent baroclinic zones (Laing and Fritsch 1997, 2000; Feng et al. 2019). One of these hot spots is over the east of the U.S. Rocky Mountains, where frequent MCS occurrences are observed in the afternoon and/or evenings. Most of these MCSs propagate eastward after their formation and provide heavy rainfall over the Great Plains, accounting for 30%–70% of warm season rainfall in the region between the Rocky Mountains and Mississippi River (Fritsch et al. 1986; Feng et al. 2016). These water resources generated by MCSs are essential for agriculture productivity, especially over the northern rainfed farming regions. On the other hand, these MCSs also produce an assortment of hazardous weather events over this region under certain conditions. For instance, a slow-moving or stalling MCS could lead to flash flooding or sometimes widespread river flooding, which is often accompanied by damaging winds, and prodigious lightning rates (Laing and Fritsch 2000; Schumacher and Johnson 2006; Houze et al. 2015; Feng et al. 2018). This typically happens when the upper jet stream is relatively weak and/or the low-level jet is oriented toward the west or southwest edge of the MCS (Corfidi 2003). Such a condition impedes the eastward propagation of MCSs. As a result, new storms form

Supplemental information related to this paper is available at the Journals Online website: https://doi.org/10.1175/JCLI-D-22-0529.s1.

Ming's current affiliation: Schiller Institute for Integrated Science and Society and Department of Earth and Environmental Sciences, Boston College, Boston, Massachusetts.

Corresponding author: Wenhao Dong, wenhao.dong@noaa.gov

DOI: 10.1175/JCLI-D-22-0529.1

over the same area, bringing repeated rounds of heavy rain. One notable example is the Great Flood of 1993, which was caused by voluminous rainfall along the Mississippi and Missouri Rivers produced by persistent and repetitive MCSs (Junker et al. 1999).

MCSs undoubtedly constitute an important subject as one strives to understand and predict the mean climate and extreme weather. However, despite decades of efforts to improve model performance, MCSs remain difficult to simulate in general climate models (GCMs) (Donner 1993; Donner et al. 2001; Mapes et al. 2006; Moncrieff and Liu 2006; Moncrieff et al. 2012, 2017; Feng et al. 2018; Moncrieff 2019). The lack of the simulated MCSs is deemed as one of the major reasons for the long-standing precipitation bias over the central United States as found in many generations of regional and global climate models (Klein et al. 2006; Lin et al. 2017). The vertically tilted MCS-like circulations (referred to as slantwise layer overturning) that occur across multiple scales are challenging for GCMs. The scale-separation assumptions (small cumulus scale versus the large-scale motion) used in deep convection parameterizations fail to recognize mesoscale dynamics manifested in MCSs (Moncrieff 2004, 2010; Moncrieff et al. 2017; Lin et al. 2019). A multiscale coherent structures parameterization (MCSP) scheme was proposed to fill in this gap (Moncrieff et al. 2017; Moncrieff 2019). This scheme is developed specifically to better represent MCSs in GCMs. It adds mesoscale momentum transport and top-heavy convective heating terms, which are observed in organized convection, to the existing deep convection parameterization while keeping the column heat budget unchanged. The implementation of the MCSP scheme in the DOE Energy Exascale Earth System Model (E3SM; Golaz et al. 2019) led to considerable improvement in simulating tropical waves and Madden–Julian oscillation (Yang et al. 2019; Chen et al. 2021). However, it only shows some minor impacts on the simulated MCSs over the United States (Xie et al. 2020), indicating more careful evaluation and coordinated adjustment of different schemes are needed in future studies. In addition to the MCSP scheme, another widely adopted approach is the multiscale modeling framework (MMF), also known as superparameterization, in which a cloud-resolving model is embedded in each GCM grid column to replace the cumulus parameterizations (Grabowski and Smolarkiewicz 1999). This framework has shown some improvements in simulating MCS-like features over the continental United States, but large underestimations of their occurrence frequencies still exist (Yang et al. 2017; Feng et al. 2018; Lin et al. 2019, 2022). Similar problems can be found in regional convection-resolving models, where the diurnal cycle of precipitation is improved but the simulated features of MCSs vary from the observation (Clark et al. 2007; Davis et al. 2003; Prein et al. 2020). Moreover, these simulations are computationally expensive and are only available for a few years. As an alternative configuration, a variable-resolution approach, in which higher resolution is used over a region of interest with a gradual transition to coarser resolution elsewhere, has been explored to study regional processes at a relatively lower computational cost. For instance, Feng et al. (2021a) evaluated MCS features over the United States based on two sets of 10-yr variable resolution experiments using the Community Earth System Model (CESM; Gettelman et al. 2018). Although finer resolutions (50 and 25 km) were centered over North America, the number of simulated MCSs in the central United States was significantly underestimated (>50%) in both experiments.

Despite these deficiencies, a valuable point as highlighted by a few studies outlined above is that GCMs with grid spacing finer than 100 km have the potential for substantial improvements in the synoptic-scale environment, which are argued to have important impacts on modeling MCSs and their characteristics. This viewpoint is consistent with previous studies on tropical cyclone simulations that moderately high resolution (tenths of kilometers) is capable of simulating multiple tropical cyclone statistics (e.g., Zhao et al. 2009). And it would be important to evaluate the model performance when the variable-resolution (e.g., 50 km over North America) model is extended to a global higher-resolution (50-km) model despite the limitations of this resolution. In this work, we evaluate the MCS statistics simulated by a global ~50-km atmospheric GCM developed at GFDL (Zhao 2020). The manuscript will proceed as follows. Section 2 outlines the observational dataset, atmospheric GCM, and MCS detection and tracking algorithm. Section 3 provides a detailed evaluation of a variety of simulated MCSs features by comparing them with the observation. A discussion and conclusions are given in section 4.

2. Methods

a. Observational dataset

The 3-hourly Cloud Archive User Service (CLAUS) multisatellite infrared brightness temperature (T_b) dataset (1/3° × 1/3° horizontal resolution) during 1985–2008 (Hodges et al. 2000) is used to identify and track tropical MCSs (see the detection and tracking algorithm in section 2d). This dataset has been used in various studies of MCSs and validated across different climate regimes (Huang et al. 2018; Nguyen and Duvel 2008; Zhao 2022). Composites of large-scale circulation patterns associated with MCSs are constructed to investigate the favorable condition for the MCS genesis based on ERA5 reanalysis (~31 km; Hersbach et al. 2020). In addition, we use the 3-hourly Multi-Source Weighted-Ensemble Precipitation version 2 (MSWEP V2; Beck et al. 2019) gridded precipitation dataset (0.1° × 0.1° resolution) to explore the MCS-related precipitation. To facilitate a model–observation comparison, all the observational datasets are interpolated onto the model resolution.

b. Model simulations

A finer-resolution version (referred to as C192AM4; Zhao 2020) of the atmospheric model AM4 (Zhao et al. 2018a,b) is used in this study. The default AM4 model has cubed-sphere topology with 96 × 96 grid boxes per cube face (approximately 100-km grid size). C192 represents 192 × 192 grid boxes in each of the six cubed-sphere faces, which is equivalent to ~50-km horizontal grid spacing. This model was used for GFDL's participation in the Coupled Model Intercomparison Project Phase 6 (CMIP6) HighResMIP project (Haarsma et al. 2016). The physical parameterizations in the AM4 model include a "double-plume" convective closure scheme to represent both shallow and deep convection (Zhao et al. 2016). The turbulent diffusivity in the planetary boundary layer is

parameterized following Lock et al. (2000). The cloud microphysics is a single-moment bulk scheme based on the works of Rotstayn (1997) and Jakob and Klein (2000). The longwave radiation code adopts the simplified exchange approximation with the latest spectroscopy and inclusion of the 10-μm CO_2 band (Schwarzkopf and Fels 1991). The shortwave code employs the 18-band formulation with updated H_2O, CO_2, and O_2 formulations and inclusion of the shortwave water vapor continuum and CH_4 and N_2O absorption (Paynter and Ramaswamy 2012, 2014). Orographic gravity wave drag is parameterized following the works of Garner (2005) and Garner (2018). Nonorographic gravity wave drag is parameterized following Alexander and Dunkerton (1999). Compared to the default AM4, there are a few modifications made to this high-resolution version. As detailed in Zhao (2020), the model's physics and dynamics time steps have been adjusted due to the increase in the horizontal resolution. The C192AM4 has a gravity wave and Lagrangian dynamics step of 75 s, a vertical remapping and horizontal advection step of 600 s, and a physics and land model step of 1200 s. Besides, a fourth-order instead of a sixth-order divergence damping is used to increase the model's numeric stability. In addition, the cloud parameterization is tuned to increase the top-of-atmosphere radiative fluxes, which aims to reduce the cold bias in coupled model simulations of the historical sea surface temperature. We use a three-member ensemble to evaluate the simulated MCSs over the United States in the present-day climate covering 1950–2014 (referred to as C192AM4-PD). These simulations are driven by the observed SST and sea ice conditions, greenhouse gases, and natural and anthropogenic aerosol emissions. The three members are generated by slightly perturbing the model's initial condition. Outputs from these simulations have been used to evaluate several important weather phenomena, such as the atmospheric rivers, tropical cyclones, and MCSs (Zhao 2020; Dong et al. 2021; Zhao 2022). The results have shown that this model is capable of simulating these systems reasonably well. The model outputs for single-level variables such as precipitation and the top of atmosphere outgoing longwave radiation (OLR) are saved at 3-h intervals, while those for multiple-level variables such as temperature, horizontal winds, and geopotential height are saved at 6-h intervals. All the analyses performed in this study cover 1985–2008 to coincide with the CLAUS dataset.

c. Conversion from OLR to T_b

Following our previous works (Dong et al. 2021; Zhao 2022), the simulated brightness temperature (T_b) is calculated based on the OLR by the following equations:

$$\begin{cases} T_F = T_b(a + bT_b) \\ \text{OLR} = \sigma T_F^4 \end{cases},$$

where T_F is the flux equivalent brightness temperature, $\sigma = 5.67 \times 10^{-8}$ W m^{-2} K^{-4} is the Stefan–Boltzmann constant, and a and b are empirical coefficients fitted based on the above equations. The fitted values of a and b are 1.283 and -1.281×10^{-3} K^{-1}, respectively, in this study. As shown in Fig. 1, the simulated annual and warm season mean T_b agrees well with the CLAUS observations, with the centered pattern correlations over the continental United States larger than 0.98 ($p < 0.001$). Larger values of T_b are observed over dry regions like the deserts over the southern United States. The values generally decrease northward as higher latitudes are increasingly obscured by clouds. Also obvious are the high and cold Rocky Mountains where smaller T_b are observed. The difference between the observation and model simulation reveals that the simulated T_b is overestimated by a few degrees over the northern Great Plains while it is slightly underestimated over the western and southeastern United States. When averaged over the entire continental United States, the root-mean-square error of the simulated annual (warm season) T_b is 1.2 K (1.5 K).

d. MCS detection and tracking algorithm

The MCS detection and tracking method follows that in Dong et al. (2021). Here is a brief summary of this two-step algorithm. It first identifies MCS candidates based on a T_b threshold and a minimum area coverage threshold, which are set to 221 K and 30 000 km^2, respectively, in this study. These two (or similar) values have been used extensively to detect MCSs over the United States in previous studies based on automated tracking algorithms (Maddox 1980; Anderson and Arritt 2001; Feng et al. 2019; Cheeks et al. 2020). Slight changes in these two thresholds have no bearing on the main conclusions of this study. After initial identification, a tracking procedure is performed to link those identified objects. Candidates in consecutive timeframes with more than 15% overlapping area are classified as the same MCS. For small or fast-moving MCSs with no sufficient overlapping between two timeframes, the tracking procedure invokes a Kalman filter approach to provide an estimate for the movement of potential MCSs. More details of the algorithm and comparison with other algorithms can be found in Huang et al. (2018). The center of each identified MCS is defined by its centroid computed based on grid points covered by area with T_b lower than the threshold.

3. Results

a. Typical cases and long-term means

Figures 2–4 show two typical eastward propagating MCSs, one observed and one simulated by the model. They are randomly selected for illustrative purposes. Their tracks are shown in Fig. 1 with their genesis locations marked as red dots. Both cases originate in the evening [0000 UTC (1800 LST)] to the east of the Rocky Mountains, and both are large (mean size larger than 16×10^4 km^2) and long-lived MCSs (lasting for 24 h). The observed case was first detected at 0000 UTC 8 June 2005 near the borders of North Dakota and South Dakota. It is a typical asymmetric MCS based on Houze et al.'s (1990) categorization. As it is evident in the radar reflectivity plot shown in Fig. 3, one can see clearly that the convective line is stronger on its southern end while the stratiform region is located toward its north end rather than centered behind it. The detection results confirm the robustness and effectiveness of the tracking method. The simulated case detected at 0000 UTC 28 May 2007 illustrates a merging

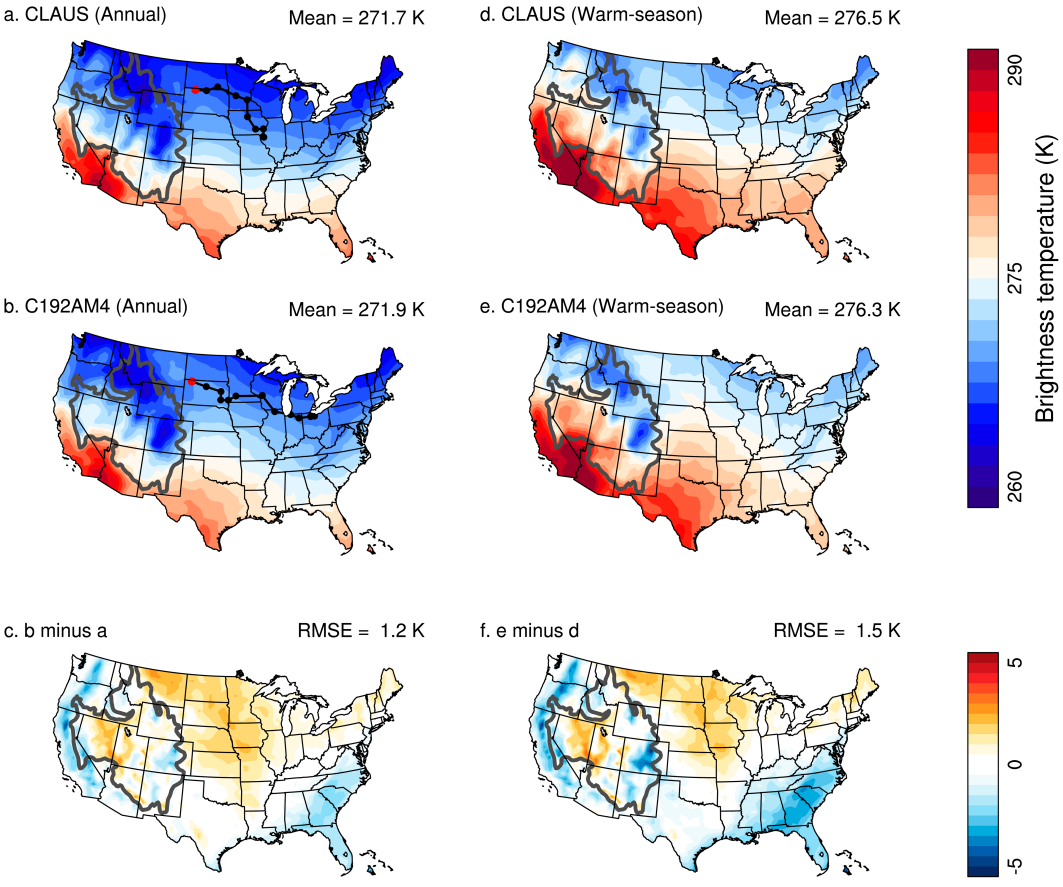

FIG. 1. Spatial distribution of (left) annual and (right) warm season (April–August) mean brightness temperature (K) from (a),(d) CLAUS and (b),(e) C192AM4-PD for 1985–2008. (c),(f) Differences are shown: (c) is (b) minus (a) and (f) is (e) minus (d). The mean value or the root-mean-square error is shown on the top right of each panel. The black solid line with dots in (a) and (b) indicates a typical mesoscale convective system (MCS) in both observation and model simulation, which are shown in Fig. 2. Red dots indicate the genesis location. The thick gray isoline marks the 1500-m contour of surface elevation, which is used to delineate the Rocky Mountains.

process of two individual clusters. An identified MCS was located near the borders of Wyoming, South Dakota, and Nebraska and another weaker cluster was located in Colorado. These two clusters merged as a bigger MCS a few hours later near the borders of South Dakota, Nebraska, Minnesota, and Iowa. It then kept propagating southeastward before it decayed over Wisconsin.

The observed and simulated long-term annual mean occurrence (track density) and genesis (first record along each MCS's track) frequency of MCS over the United States as well as their differences are shown in Fig. 5. Given the frequent occurrence of MCS during the warm season, which spans from April to August, we also restrict our analysis on this period. To account for the varying large-scale environments associated with MCS occurrence, as reported in previous studies (Song et al. 2019; Prein et al. 2020; Feng et al. 2021a), we further divide the warm season into two distinct periods: spring to early summer (April–June) and late summer (July–August). The MCS occurrence and genesis frequency are calculated by averaging the respective monthly total over all 24 years for each grid point. Consistent with many other observational studies (Feng et al. 2019; Cheeks et al. 2020), the annual mean occurrence frequency of MCSs is high over the central United States between the Rocky Mountains/Colorado Plateau and the Appalachian highlands, with a secondary maximum center along the southern coastal states (Texas, Louisiana, Mississippi, Alabama, and the Florida Panhandle) (first row of Fig. 5). These features are particularly prominent during the warm season, with the occurrence frequency of MCS being twice as high in the spring and early summer months compared to the late summer period. The ensemble mean of C192AM4-PD simulations generally captures the observed spatial distribution of the annual mean frequency of MCSs, with a centered pattern correlation of 0.6 ($p < 0.001$) over the United States (second row of Fig. 5). Note that the differences among the three ensemble members are small. All the regions with active MCS occurrences in observations feature prominently in the simulation. However, the differences between observation and model simulation reveal that although their differences are small over the central United States and the southern coastal states, the simulated track density of MCSs is substantially overestimated

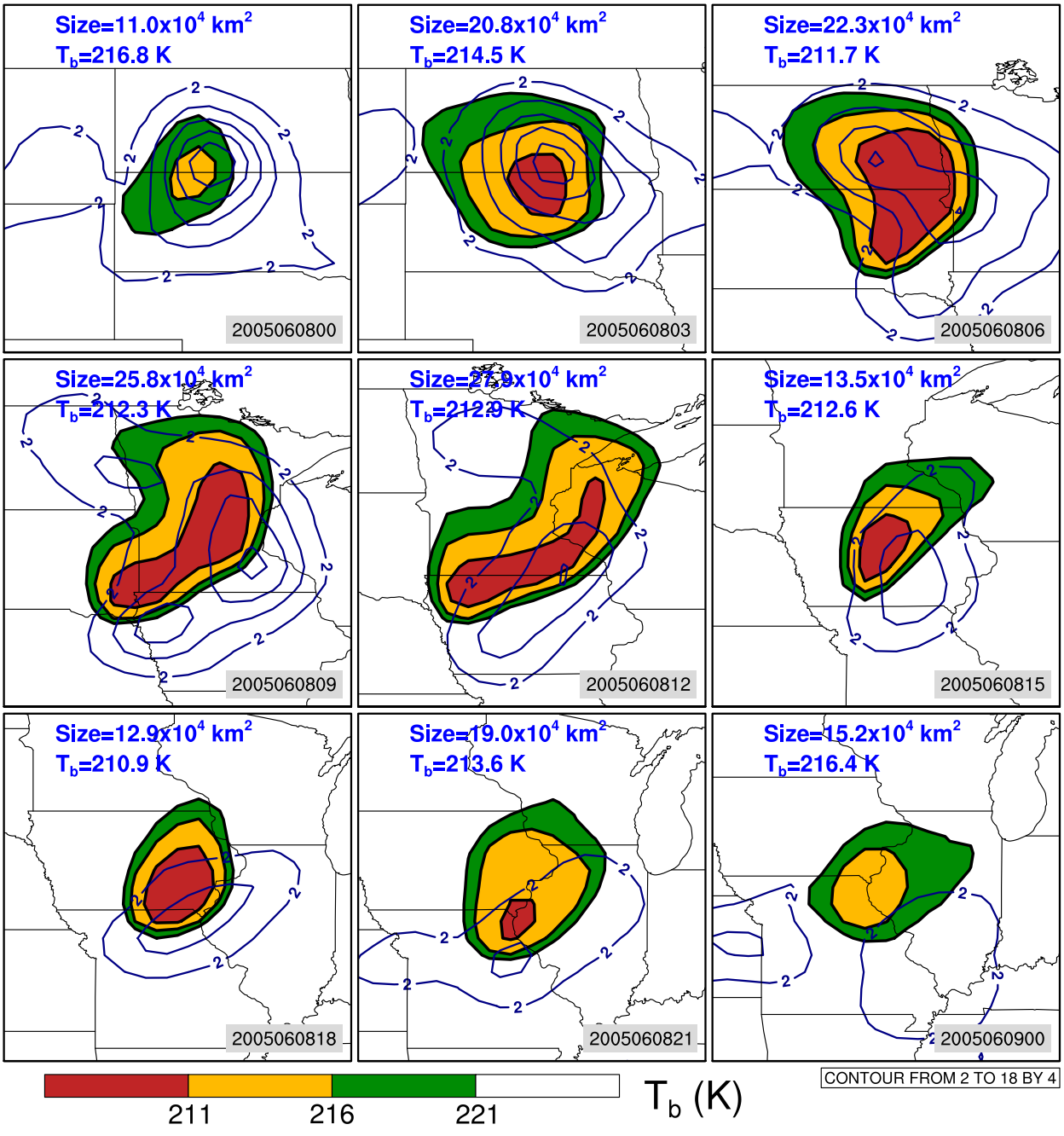

FIG. 2. An observed typical MCS observed covering 0000 UTC 8 Jun 2005–0000 UTC 9 Jun 2005. The shading shows the brightness temperature (K) based on the CLAUS dataset. The contour shows the precipitation (mm day^{-1}) based on the MSWEP dataset ranging from 2 to 18 with an interval of 4. The center of each panel represents the location of MCS at that time step while the track of this case is shown in Fig. 1b. The size and averaged brightness temperature for each time frame are shown in each panel.

over the eastern United States (third row of Fig. 5). The model also produces biased more MCSs over the U.S. Southwest stretching from the eastern Colorado plains to New Mexico. This bias is present in both warm season subperiods, with a greater bias during the spring and early summer months.

The occurrence frequency of MCSs depends on both genesis and duration. Here we first examine their genesis frequency and shall discuss their duration in section 3c. Most of the observed MCSs are generated between the Rocky Mountains and the Mississippi River (Fig. S1 in the online supplemental material). Similar to the occurrence frequency, the model reasonably reproduces the genesis frequency of MCSs over the central United States and southern coastal states, while substantially overestimating it over the eastern United States, the Colorado

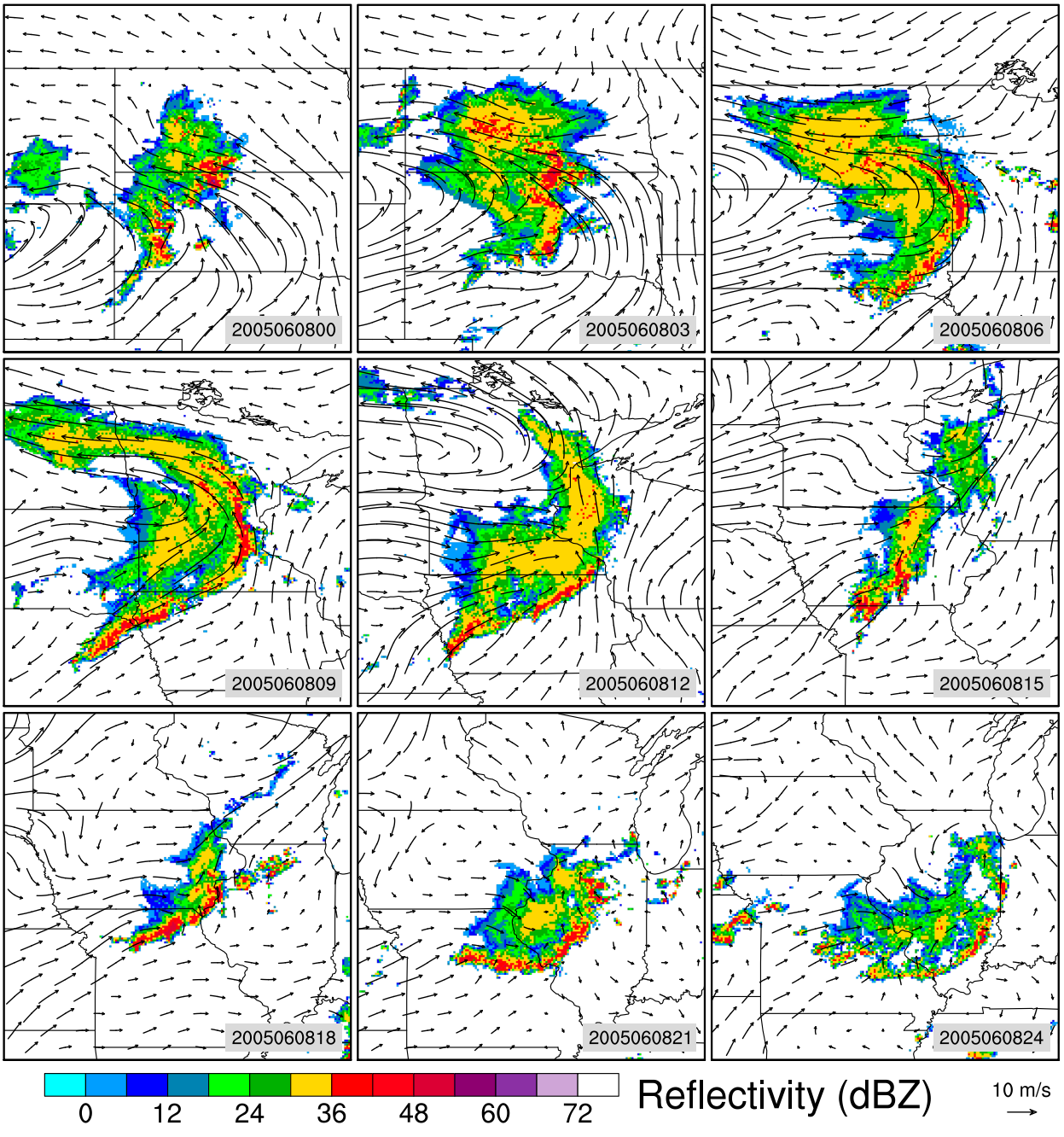

FIG. 3. As in Fig. 2, but for the radar reflectivity (shading; dBZ) at the 0.5° elevation angle based on the NOAA WSR-88D network and the 700-hPa horizontal wind anomalies (vectors; m s^{-1}). The precipitation (contours; mm day^{-1}) shown in Fig. 2 is also plotted for a reference.

plains, and New Mexico. When summed over the central United States (black rectangle in Fig. 5a), the model overestimates the annual occurrence frequency by 9% (433 vs 471), and the overestimation is about 15% (91 vs 105) for genesis frequency. The corresponding values for the spring and early summer are 8% and 17%, respectively, while they are −10% and −8% for the late summer period.

b. *Seasonality, interannual variability, and diurnal cycle*

This section focuses on the variability of MCS on different time scales. Figure 6 compares the simulated seasonal cycles of occurrence and genesis frequency of MCSs with the observations averaged over the central United States where the most frequent MCS activities are observed. Overall, the

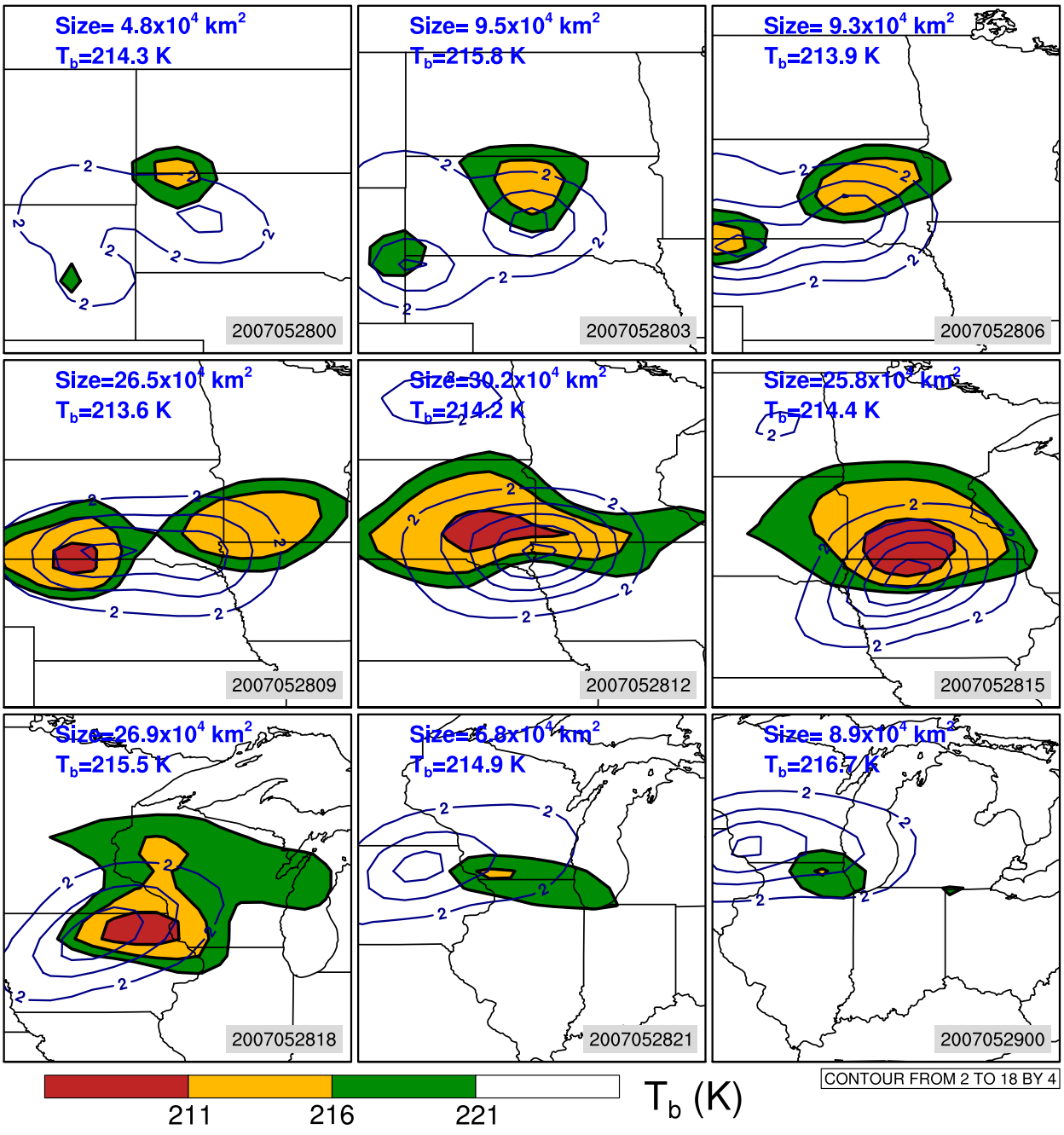

FIG. 4. As in Fig. 2, but for a simulated typical MCS covering 0000 UTC 28 May 2007–0000 UTC 29 May 2007.

model shows considerable skill in capturing the amplitudes and phases of the observed seasonal cycles of MCS occurrence frequency (Fig. 6a). The ensemble mean largely falls within one standard deviation of the observations. The correlation coefficients between the simulated and observed seasonal cycle of MCS occurrence frequency are statistically significant ($R > 0.93$; $p < 0.001$) for all three members. The seasonal cycle of MCS genesis frequency shares a large similarity with the occurrence frequency although the absolute value is smaller by a factor of 5 (Fig. 6b). Consistent with previous studies (Anderson and Arritt 2001), both occurrence and genesis frequency of MCSs are concentrated in warm season (April–August) while their frequencies are relatively lower in other months. Therefore, unless otherwise stated, we shall focus on the warm season in the following analysis. To account for different large-scale environments associated with MCS occurrence (Song et al. 2019; Prein et al. 2020; Feng et al. 2021a), the warm season is further

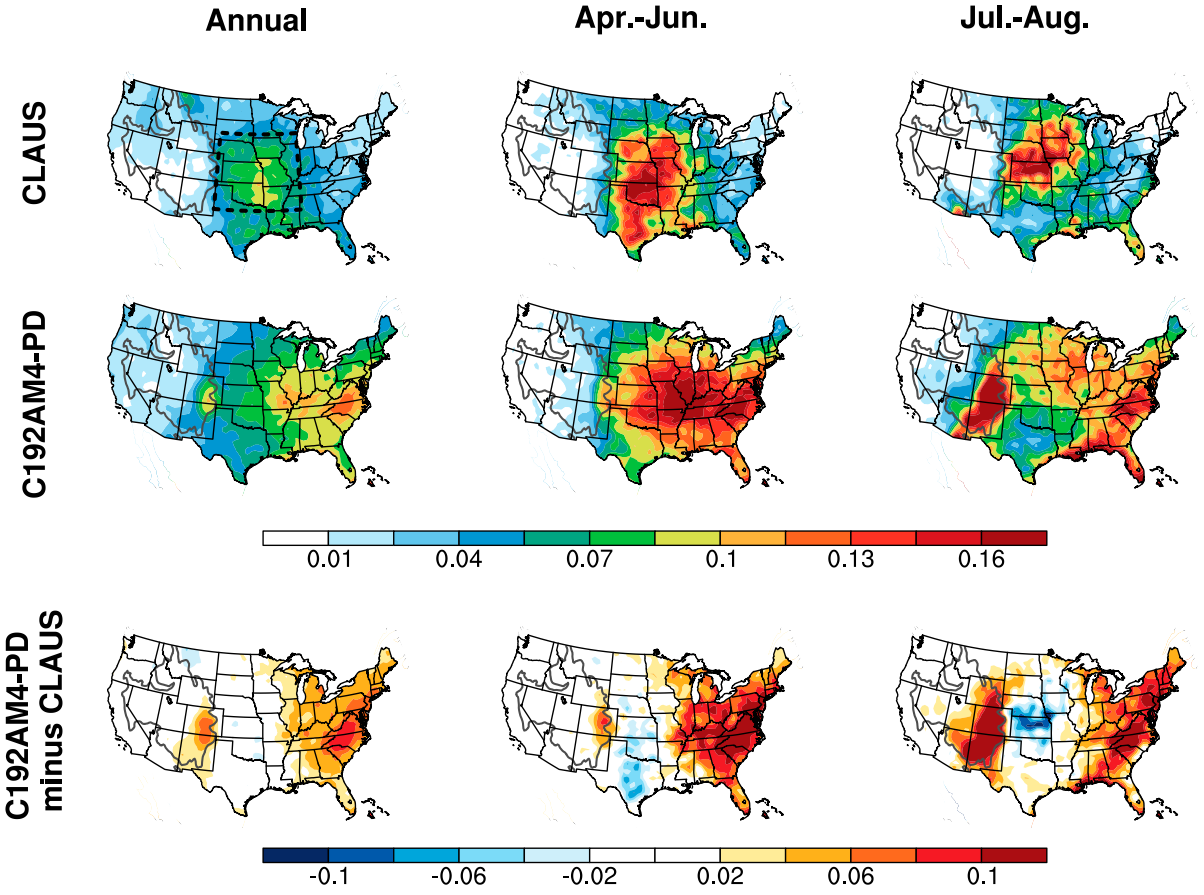

FIG. 5. Occurrence frequency (fraction per month per grid) of MCSs based on (top) CLAUS and (middle) C192AM4-PD for 1985–2008 during the (left) whole year, (center) spring and early summer, and (right) late summer. (bottom) The difference between C192AM4-PD and CLAUS. Thick gray contour in all panels denotes the 1500-m isoline. The black dashed rectangle in the first panel denotes the central U.S. region used for the subsequent analysis.

divided into two periods: spring to early summer (April–June) and late summer (July–August).

Figure 7 concerns the interannual variability of MCS activities averaged over the central United States in two subperiods. The simulated mean values and the year-to-year fluctuation of MCS occurrence frequency are comparable with the observation (see statistical numbers listed in the figure) although the correlation coefficients between them are low (first column of Fig. 7). This

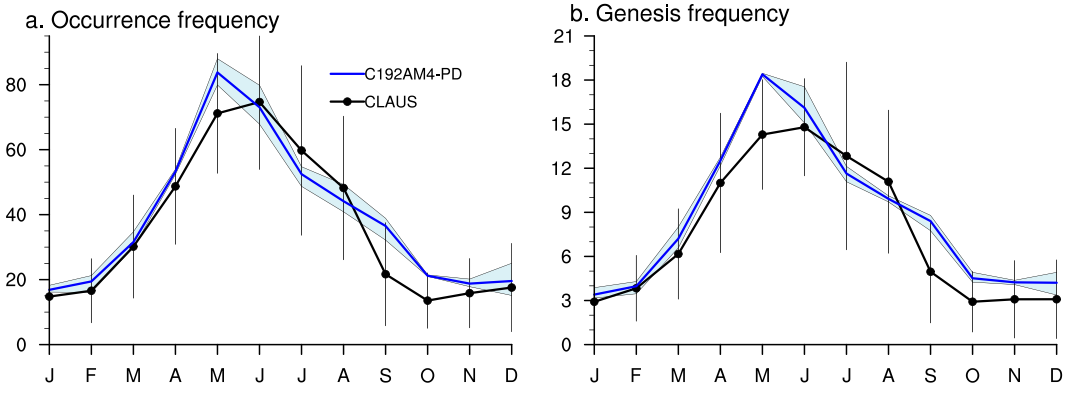

FIG. 6. Observed (CLAUS; black) and simulated (C192AM4-PD; blue) seasonal cycles of (a) occurrence and (b) genesis frequency (number of occurrences) of MCSs averaged over central United States defined by the black dashed rectangle in Fig. 5. The light blue shading denotes the spread among the three ensemble members.

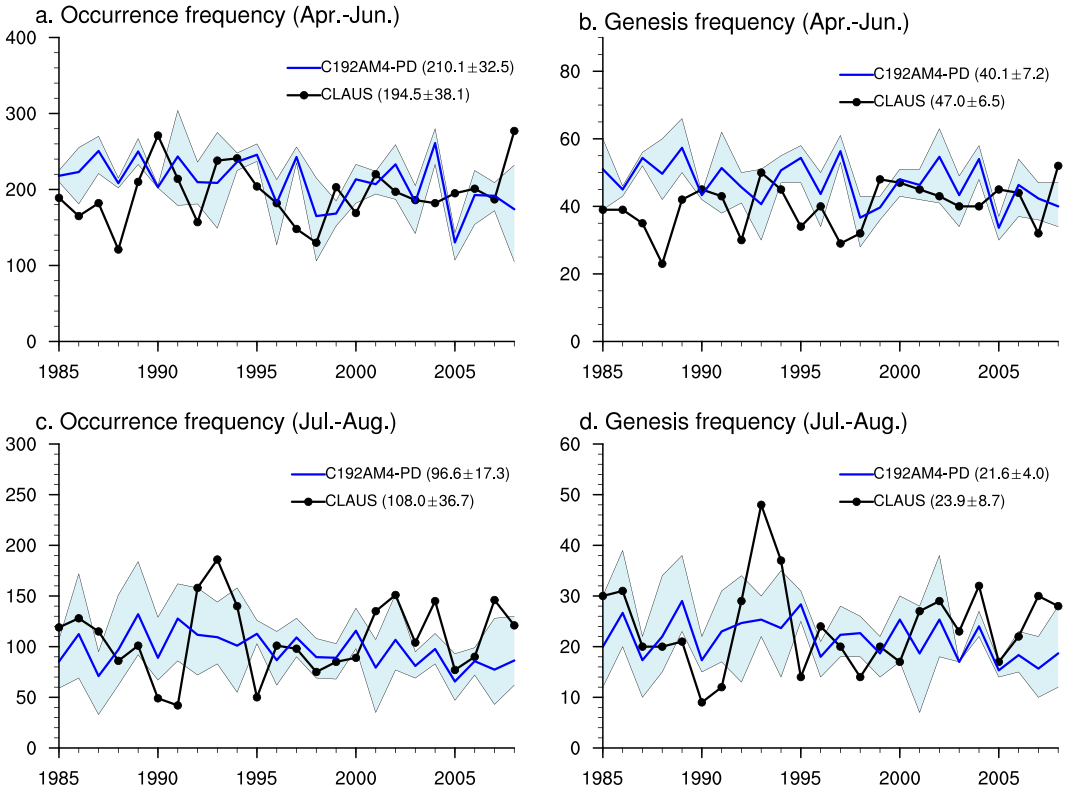

FIG. 7. Observed (CLAUS; black) and simulated (C192AM4-PD; blue) interannual variations of (a),(c) occurrence and (b),(d) genesis frequency of MCS averaged over central United States during (top) spring and early summer and (bottom) late summer. The respective 1985–2008 means and standard deviations are listed. The light blue shading denotes the spread among the three ensemble members.

is anticipated since year-to-year correspondence is not expected to be perfectly captured by the model given that the interannual variability might largely subject to internal variability. The three ensembles also show low to medium correlation between each other, ranging from 0.1 to 0.5. The same results can be found in the MCS genesis frequency (second column of Fig. 7). This consolidates the conclusion as summarized in Dong et al. (2021) that the interannual variability of simulated MCSs over continental regions is not determined to first order by the prescribed SST and sea ice conditions, and may instead be subject to complex land processes and atmosphere–land interactions. This is further confirmed by comparing the MCS features under the condition of different El Niño–Southern Oscillation (ENSO) phases (the largest SST signal), which shows little differences (figures not shown). Besides, convective storms across the U.S. Great Plains are found to be coupled with preexisting midtropospheric perturbations initiated over the Rocky Mountains (Wang et al. 2009, 2011). These midtropospheric perturbations are tied to the Great Plains low-level jet (GPLLJ). We compared the simulated GPLLJ with the observation at 6-h intervals averaged over the warm season. As shown in Fig. S2, the model reasonably simulates the diurnal cycle of GPLLJ, characterized by strong nocturnal (0600 UTC) southerlies over the Great Plains. However, the simulated extent and the intensity of the GPLLJ are smaller than the observation. These biases could potentially impact the creation of midtropospheric perturbations and, consequently, the genesis and propagation of MCSs.

The high-frequency datasets used in this study enable us to explore the diurnal features of MCSs. We perform a Fourier analysis on the 3-h dataset for each grid to quantify the diurnal cycle. The amplitude and phases of the first harmonic are adopted here to represent the strength of the diurnal cycle and the peak timing, respectively.

The amplitude and phase of the diurnal cycle of MCS occurrence and genesis during the two subperiods are shown in Fig. 8. Consistent with the typical case shown above, most of the observed MCS occurrences tend to become active at night and persist into the early morning hours throughout the warm season. The gradually increasing peak timing, from 1800–2300 LST (eastern Rocky Mountains) to 0000–0500 LST (central lowlands) is indicative of the eastward propagation feature of MCSs, consistent with the observed nocturnal precipitation features (Balling 1985). Most of the MCS genesis over the Great Plains occurred in the late afternoon and early evening (1700–2200 LST). These features are related to the strong diurnal heating over the Rocky Mountains and the associated mountain–plain solenoidal circulation (Carbone and Tuttle 2008). They are also found to be closely linked to the formation of a dryline, a low-level boundary commonly formed over the Great Plains region. It separates the dry air from the

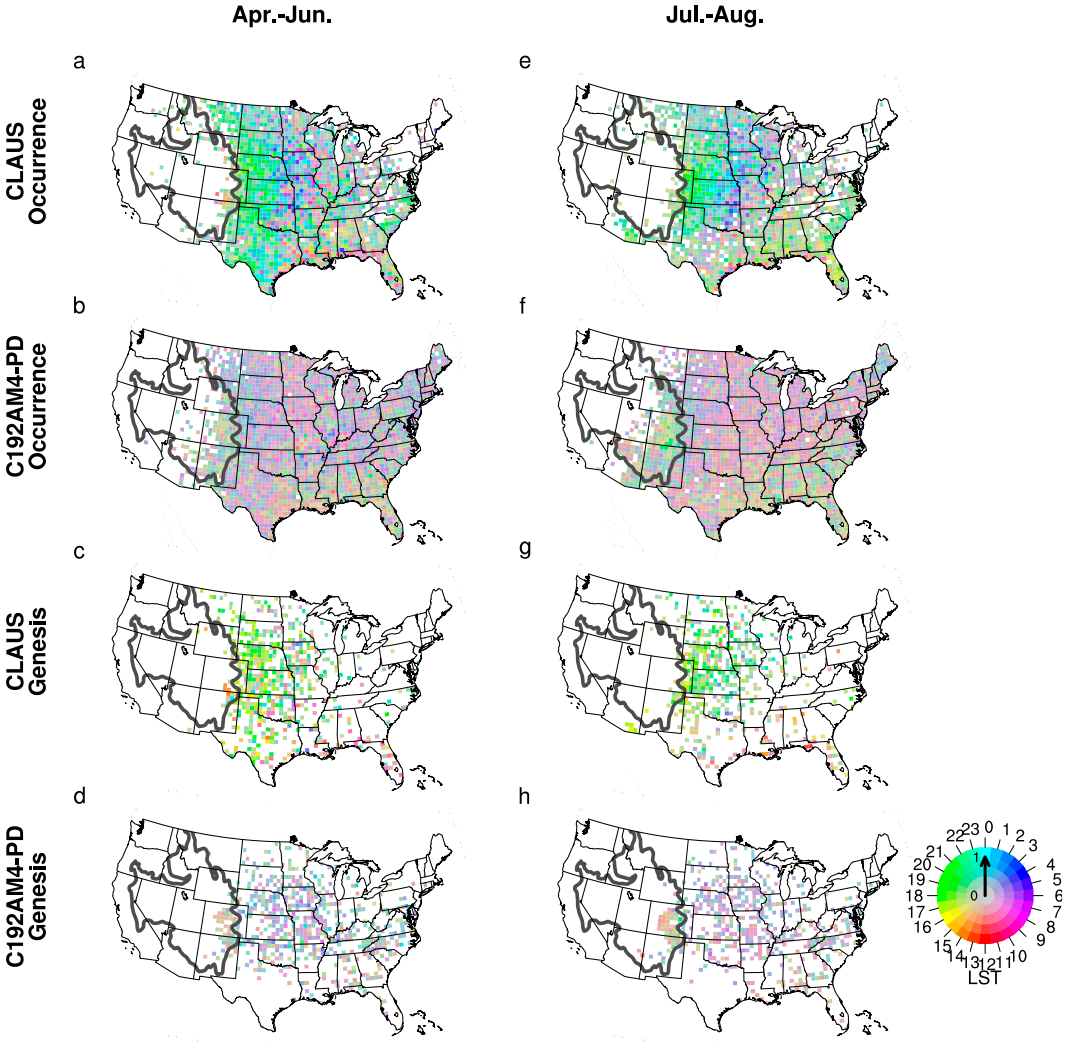

FIG. 8. Phase (hue) and amplitude (saturation) of the first diurnal harmonic of (a),(b),(e),(f) occurrence frequency and (c),(d),(g),(h) genesis frequency of MCSs based on CLAUS in (a), (c), (e), and (g) and C192AM4-PD in (b), (d), (f), and (h) for 1985–2008 during (left) spring and (right) early summer and late summer. The phase has been converted from coordinated universal time (UTC) to local solar time (LST).

west from the moist air from the Gulf of Mexico. The formation of this dryline plays an important role in convection initiation by interacting with the Great Plains low-level jet (Hoch and Markowski 2005; Mitchell and Schultz 2020). It has been pointed out that the dry air cools more quickly at night than the moist air, resulting in a west–east temperature gradient by morning hours, which favors the genesis of the MCSs (Mitchell and Schultz 2020). As shown in Fig. S3, the geneses of the observed MCS are accompanied by the presence of drylines over the central United States, characterized by dry air to the west and moist air to the east. This feature is captured by the model simulation although the intensity of the simulated dryline is slightly weaker. Over the southern coastal regions, MCSs are generated around noon and early afternoon (1100–1500 LST), which are likely associated with sea breeze convergence from strong diurnal heating over the adjacent land in the local afternoon. By contrast, the overall amplitude of the diurnal cycle is weaker in the simulations and the simulated peak timing differs largely from the observation. More specifically, the simulated MCSs over large areas of the central United States occur around the dawn time (0500–1000 LST) with the genesis time concentrated in the morning hours (0000–0800 LST). The relatively smaller changes in the peak timing across the west to the east suggest a faster mean translation speed of the simulated MCSs (see more analysis in section 3c). Over the eastern Colorado plains where the model produces too many MCSs, these systems are generated in the afternoon (1400–1500 LST). These findings suggest that the model cannot accurately represent the diurnal cycle of MCSs in the two subperiods and further model improvement would be needed.

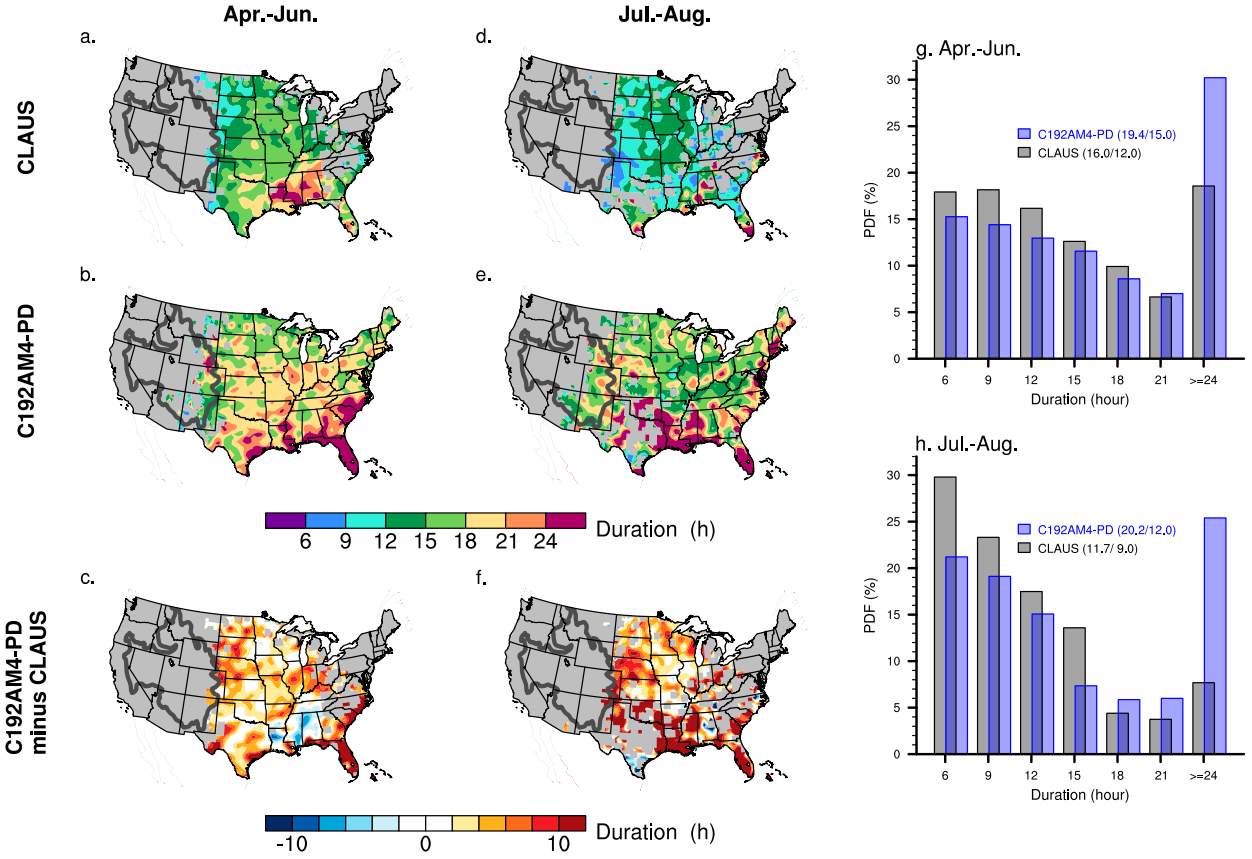

FIG. 9. Spatial distribution of MCS mean duration (h) from (a),(d) CLAUS and (b),(e) C192AM4-PD for 1985–2008 during (left) spring and early summer and (center) late summer. (c),(f) Differences are shown: (c) is (b) minus (a) and (f) is (e) minus (d). Only grids with more than three samples are shown. Observed (CLAUS; black) and simulated (C192AM4-PD; blue) histograms of MCS duration during (g) spring and early summer and (h) later summer. The respective mean/median values are listed.

c. *Duration, MCS-associated T_b, translation speed, and size*

In this section, we examine several key characteristics of MCSs, including the duration, MCS-associated T_b, translation speed, and size. Duration is an important factor for the total rain produced by an MCS. Commonly, longer-lived MCSs bring larger accumulative precipitation. The spatial distribution of MCS duration is shown in Fig. 9. During spring and early summer, most observed MCSs over large parts of the United States typically last for 12–18 h, although longer durations are observed over the southern coastal regions. In comparison, the MCS duration is generally shorter during late summer. The model, however, simulates longer-lived MCS over nearly all over the United States, especially near the coastal regions, during both subperiods. This overestimation may be affected by the MCSs generated over the surrounding oceans, where the duration of MCSs was found to be biased longer in the model (Dong et al. 2021). The histogram distribution of MCS duration with a 3-h interval over the central United States is present in Fig. 9 (the third column). Overall, the model is able to reproduce the observed monotonic decrease in probability with the duration during both subperiods but is biased toward a longer lifetime. The mean (median) duration of MCS in observation during spring and early summer is about 16 (12) h whereas they are about 19 (15) h in the model. The probability of long-lasting MCSs, defined as those last longer than 24 h, accounts for 18% of the observed MCSs but 31% in the model. On the other hand, MCSs are generally shorter-lived during late summer, with a mean duration of 12 h in observations compared to 20 h in the model. Long-lasting MCSs are less common during late summer, accounting for less than 10% of observed MCSs, but approximately 25% in the model.

We then analyze the spatial distribution and the probability density distribution of the T_b averaged over all the grid points occupied by an MCS during its lifetime during two subperiods. As shown in Fig. 10, MCSs with lower T_b values are observed over the central United States and southern coastal regions in both periods while they are mainly distributed over regions to the east of the Great Plains in the model. Compared to the spring and early summer months, the mean T_b values are smaller during late summer months. The respective differences between model simulations and observations demonstrate that the MCS-associated T_b is underestimated by about 1 K in the model over large parts of the United States,

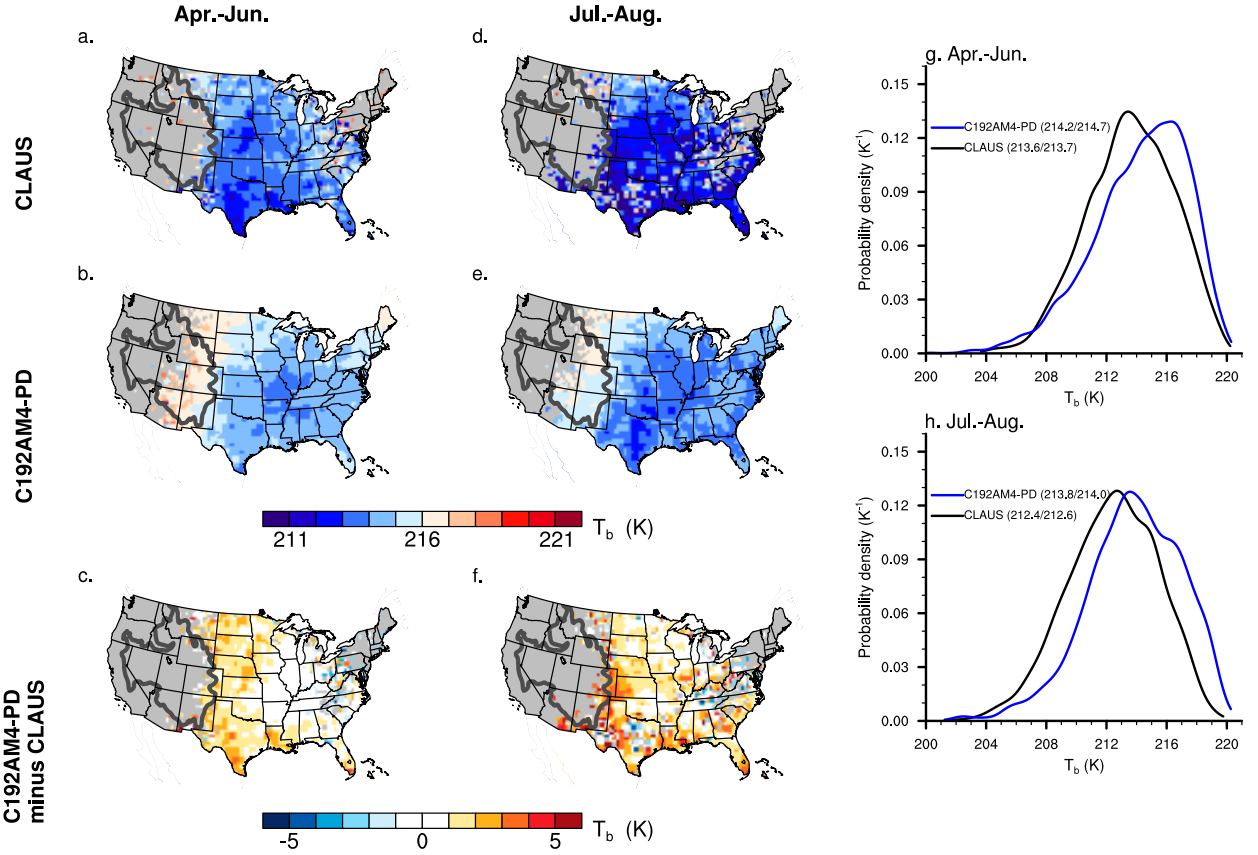

FIG. 10. Spatial distribution of MCS associated T_b (K) from (a),(d) CLAUS to (b),(e) C192AM4-PD for 1985–2008 during (a)–(c) spring and (d)–(f) early summer and late summer. (c),(f) Differences are shown: (c) is (b) minus (a) and (f) is (e) minus (d). Only grids with more than three samples are shown. Observed (CLAUS, black) and simulated (C192AM4-PD, blue) probability density distribution of MCS associated T_b during (g) spring and early summer and (h) later summer. The respective mean/median values are listed.

which may indicate that the model employed here cannot resolve the full strength of MCSs. In other words, the simulated MCSs are less penetrative than observed. Such an underestimation is also evident in the probability density distribution of T_b averaged over MCSs occurred in the central United States (third column in Fig. 10). The simulated density distribution is more skewed than the observations toward higher T_b values in both subperiods.

The overall impact of an MCS is also partly affected by how fast it moves. Figure 11 shows the observed and simulated mean translation speed and direction of MCSs during both subperiods. The observed translation speed is characterized by larger velocities (70–80 km h^{-1}) in the north and smaller values (below 60 km h^{-1}) in the south for both subperiods. The simulated velocity of MCSs is generally overestimated across large portions of the United States during the spring and early summer, but overestimated only in the northeastern United States near the Great Lakes and underestimated in the southern coastal regions during the late summer. The Appalachians act as a transition region for faster-moving MCSs on the western side and slower-moving systems on the eastern side, as observed in both the models and simulations. The histogram distribution of translation speed shows that most MCSs observed over the central United States travel at a speed of 40–60 km h^{-1} during both subperiods. This distribution is well captured by the model, despite the fact that it simulates a slightly larger mean translation speed during spring and early summer but a smaller speed during late summer (as shown in the third column of Fig. 11). On the other hand, the observed mean MCS translation vectors, especially during spring and early summer, show a curved structure centered around the Great Plains, transitioning from slightly northeastward toward southeastward. The simulated MCS movement, however, displays a larger northeastward component to the east of the Great Plains during spring and early summer, whereas it is more zonal during late summer.

As for the size of MCSs, comparatively larger MCSs are observed at the border of the Great Plains and the Midwest (Fig. 12). This region is where the MCSs approach the mature stage after their generation from the foothills of the Rocky Mountains and subsequent eastward propagations in the nocturnal hours as shown in Fig. 8. Also, MCS size during spring and early summer is larger than late summer. This simulated distribution, however, shows an eastward shift with the maximum size mainly distributed over the Midwest during both subperiods. This could stem from a combined effect of displaced

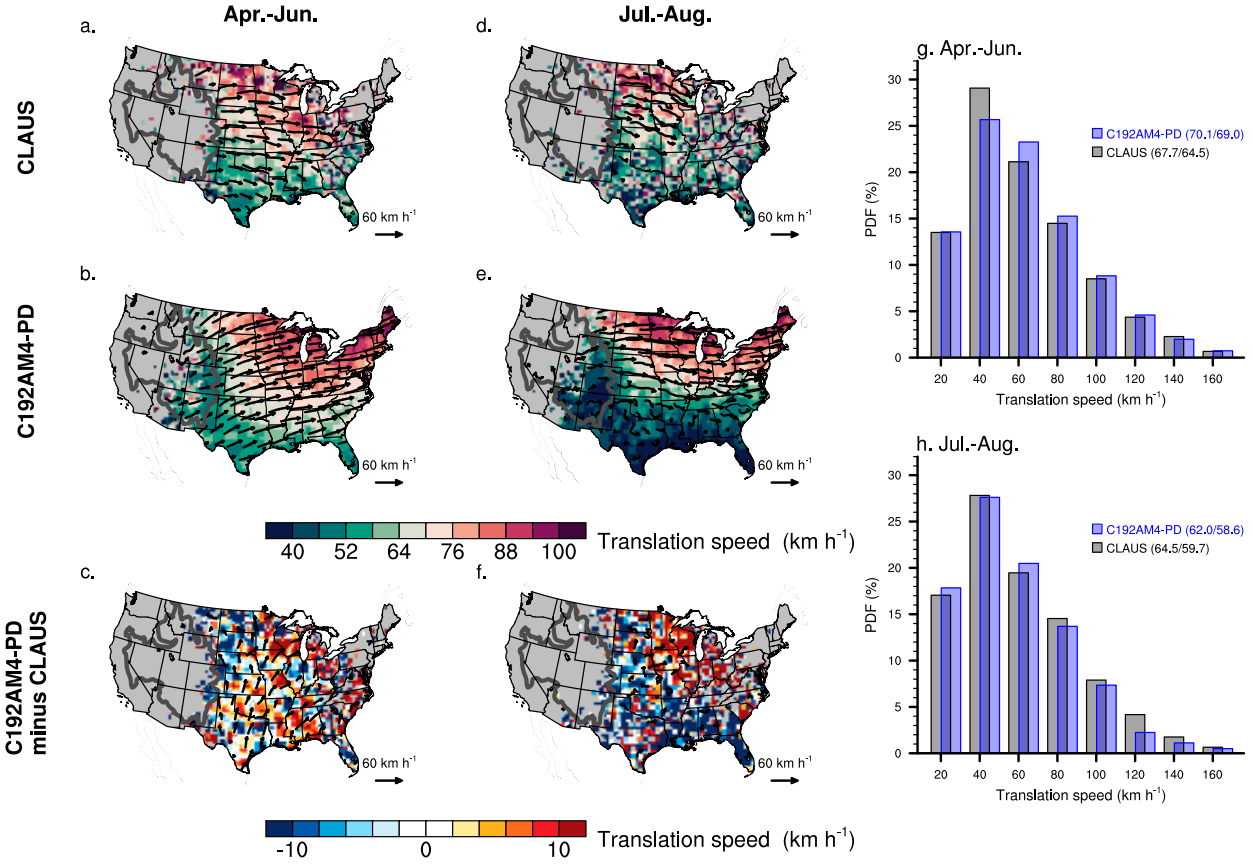

FIG. 11. Spatial distribution of MCS translation speed (shading; m s^{-1}) and direction (vectors) from (a),(d) CLAUS to (b),(e) C192AM4-PD for 1985–2008 during (a)–(c) spring and early summer and (d)–(f) late summer. (c),(f) Differences are shown: (c) is (b) minus (a) and (f) is (e) minus (d). Only grids with more than three samples are shown. Observed (CLAUS, black) and simulated (C192AM4-PD, blue) histogram of MCS translation speed during (g) spring and early summer and (h) later summer. The respective mean/median values are listed.

genesis locations, longer durations, and faster translation speed as simulated in the model. Consequently, the mean size of MCSs is underestimated over large parts of the central United States, particularly in spring and early summer, whereas it is overestimated over the eastern United States. The underestimation over the central United States is also mirrored in the probability density distributions of MCS size (as shown in the third column of Fig. 12). Both the observation and simulations are characteristic of a gamma-shaped distribution. The simulated mean and median sizes are close to the observations during both subperiods, but the model produces more smaller-sized MCSs.

In addition, previous works have shown that the size of an MCS is closely related to its duration (Machado et al. 1998; Dong et al. 2021). Specifically, longer-lived events tend to be bigger. We evaluate this correspondence based on the MCSs initiated over the central United States. Here the size of each MCS is represented by its mean values averaged over its entire life cycle. The duration–size relationship is illustrated in Fig. 13. The mean and the 95th percentile sizes are used to evaluate the dependence of MCS size on duration. The 95th percentile size is used to examine the behaviors of comparatively large MCSs, which usually make greater impacts. Results based on the observation show a strong positive correlation between MCS duration and size during the spring and early summer. The normalized rate of change is about 2% increase in mean size per 1-h increase in duration ($p < 0.005$), which is smaller than the value over tropical regions (Dong et al. 2021). The changing rate remains almost unchanged for the 95th percentile size. This robust positive duration–size relationship is clearly present in the simulation, and the normalized rates of change are comparable with the observation. However, in late summer, a negative relationship emerges between MCS duration and size, with the normalized rates of change to be small (less than 1%) except for the 95th percentile size, which experiences a larger decrease in size (2%) as duration increases. This suggests that the relationship between MCS duration and size may be influenced by seasonal factors.

d. Composite of large-scale circulation patterns

It is well established that the preferred MCS genesis location over the central United States is linked to the favorable large-scale conditions that provide both dynamical and thermodynamical

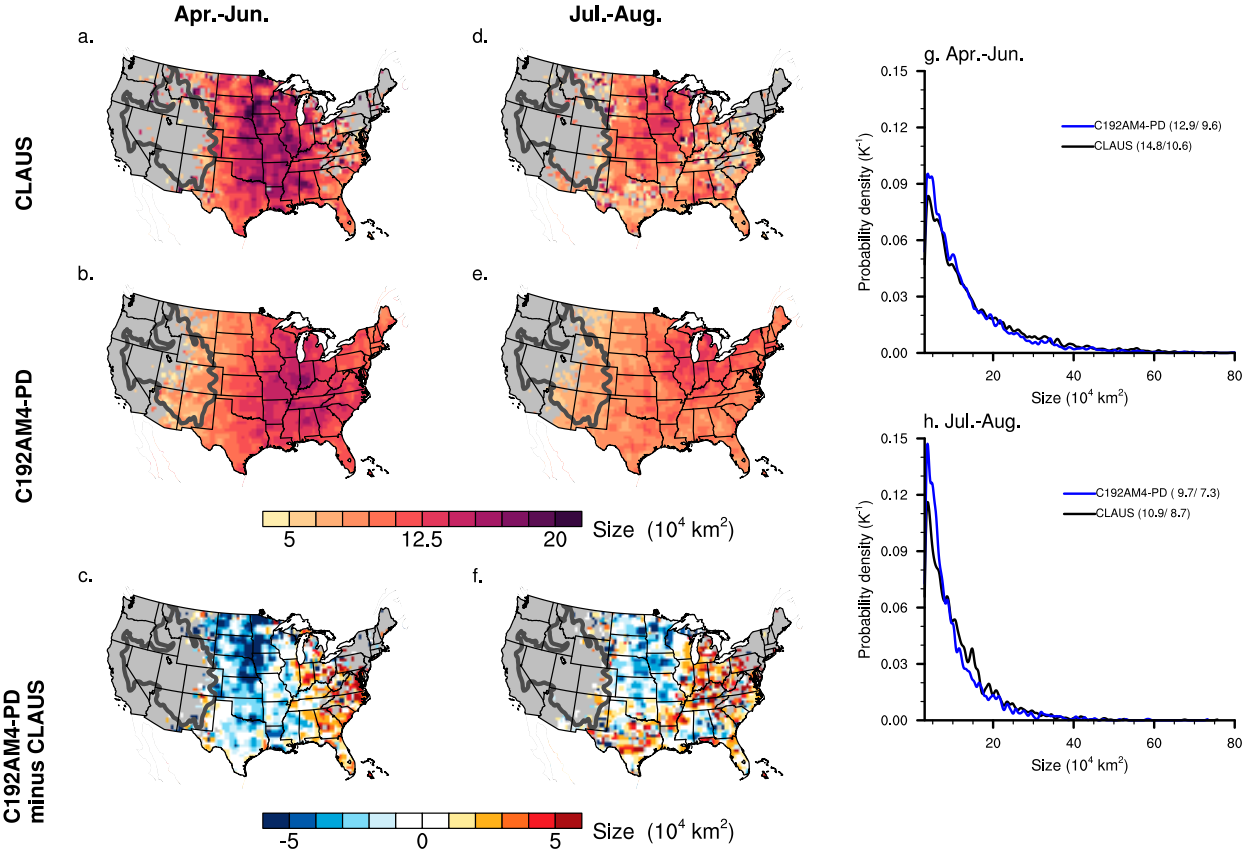

FIG. 12. Spatial distribution of MCS size (10^4 km^2) from (a),(d) CLAUS to (b),(e) C192AM4-PD for 1985–2008 during (left) spring and early summer and (center) late summer. (c),(f) Differences are shown: (c) is (b) minus (a) and (f) is (e) minus (d). Only grids with more than three samples are shown. Observed (CLAUS; black) and simulated (C192AM4-PD, blue) probability density distribution of MCS size during (g) spring and early summer and (h) later summer. The respective mean/median values are listed.

supports for their development. Using an analysis of sounding data around 10 mesoscale convective complex (MCC, an intense form of MCS) centers, Maddox (1983) found that these systems were initiated ahead of synoptic troughs embedded in the prevailing upper-level westerlies over the central United States. This was later found to be applicable to the more general MCSs by numerous follow-up studies (Coniglio et al. 2010; Peters and Schumacher 2015; Yang et al. 2017). Besides, several other influential factors have been identified, including but not limited to the low-level jet, baroclinic frontal zone, wind shear, low-level convergence, and upper-level divergence, to play significant roles in the MCS development (Trier and Parsons 1993; Laing and Fritsch 2000; Coniglio et al. 2010; Yang et al. 2017; Song et al. 2019). Moreover, previous studies analyzing long-term observations of MCSs over the United States have demonstrated distinct large-scale environments linked to the genesis and development of MCSs during the spring/early summer versus late summer periods (Song et al. 2019; Feng et al. 2021a). During spring and early summer, baroclinic waves and frontal systems are found to provide strong lifting mechanisms, while the GPLLJ delivers anomalous moisture for creating favorable dynamical and thermodynamic conditions for MCS formation and development. In contrast, during summer, while similar conditions persist, baroclinic lifting weakens while the GPLLJ strengthens. Also, MCSs form over smaller areas and shift northward during late summer in comparison to the earlier subperiods.

In this section, we construct two types of composites to evaluate the simulated large-scale conditions favorable for the MCS genesis during two subperiods. We start with the geographically fixed (Euler perspective) composites. Figure 14 compares the observed and simulated mean geopotential height, horizontal winds, and equivalent potential temperature (θ_e) at 250, 500, and 850 hPa composited on the time when MCSs are generated over the central United States. The generation time of each MCS is determined by its first recorded occurrence along its track, with each MCS having a unique generation time. The long-term means are then calculated by averaging over these generation times. The composites are generated by averaging the deviations from the corresponding time mean for each 3-h interval of the day and for each month at each grid point. This region not only has most of the MCS genesis but also has similar climatological conditions. The long-term means of these variables are well simulated in the model (figures not shown).

One striking feature during the spring and early summer months is the observed GPLLJ as indicated by the strong southerly inflows from the Gulf of Mexico at 850 hPa, which

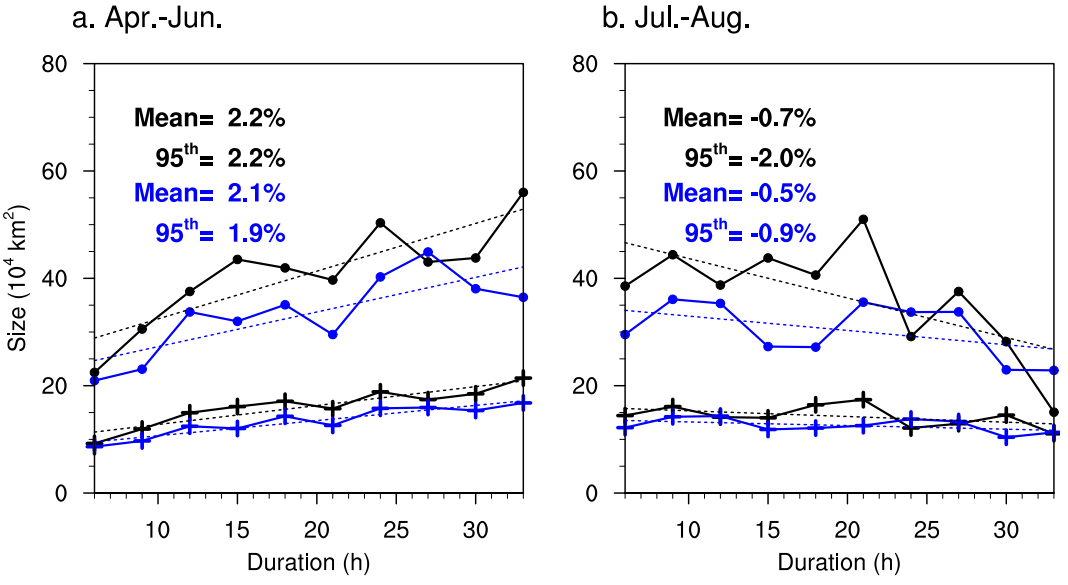

FIG. 13. Observed (black) and simulated (blue) relationships between MCS duration (h) and size (10^4 km^2) over the central United States during (a) spring and early summer and (b) later summer. The lines with cross markers are for the mean size, and the lines with solid dots are for the 95th percentile size. The dashed lines are the best linear fits. The normalized rates of change (% h^{-1}) are listed for the mean and 95th percentile size.

brings abundant moist and warm air (high θ_e values) into the central United States (Fig. 15e). Figure S2 shows that the model generally reproduces the observed diurnal cycle of the GPLLJ. However, the simulated GPLLJ veers too quickly, leading to a southward contraction and eastward extension of low-level moisture distributions (Fig. S3). This discrepancy could potentially impact the genesis and propagation of the MCSs, contributing to the large biases seen over the eastern United States. Another outstanding feature is the trough–ridge pattern that is clearly present at all three levels, with the trough located to the west of the MCS initiation region (first row of Fig. 14). The trough–ridge system is closely related to the prevailing upper-level jet, the core of which contains winds in excess of 30 m s^{-1}. The entrance region of the upper-level jet is located to the northeast of the central United States, which is evident as the wind vectors there are larger and the gradient is tighter. Consequently, upper-level divergence and lower-level convergence are observed to the right rear of the entrance region (figures not shown). The low-level convergence together with divergence aloft indicates strong dynamical rising motion over the central United States ahead of the trough. The ascending motion elevates the moist air in the boundary layer transported by the GPLLJ throughout the troposphere, providing favorable conditions for upscale growth and maintenance of MCSs.

The simulated distributions of these composites (second row of Fig. 14) agree well with the ERA5 reanalysis (first row of Fig. 14). And most of the observed features are reliably captured by the model, but the simulated upper-level jet is relatively weaker. This is mirrored in smaller gradients in the geopotential height and θ_e contours at 250 hPa compared to the ERA5 reanalysis. Moreover, the simulated GPLLJ does not penetrate northward as far as observed; instead, it turns northeastward at lower latitudes with stronger zonal components. This might be caused by the stronger North Atlantic subtropical high simulated in the model, which drives larger easterly but smaller southerly components over the central United States. These biases might contribute to the more concentrated MCS occurrence to the east of the central United States in the model as shown in Fig. 5. In contrast, during the late summer months, the previously mentioned features remain present but the trough–ridge patterns shift northward due to the strengthening of the North Atlantic subtropical high and the retreat of the upper-level jet (third row of Fig. 14). Consequently, weaker rising motion is anticipated over the central United States when compared to the spring and early spring. The model has captured the overall pattern, but the simulated upper-level jet is relatively weaker, and the North Atlantic subtropical high is stronger (fourth row of Fig. 14).

All the prominent features discussed above as well as their differences between ERA5 reanalysis and model simulations are also apparent in their respective anomaly fields (Fig. 15). Here, anomalies are calculated as deviations from the corresponding time mean for each 3-h period of the day and for each month at each grid point to remove the seasonal and diurnal variations. A distinct northwest–southeast alternating positive and negative geopotential height anomaly pattern is evident over the United States at all three levels during the spring and early summer months. There is a westward and poleward tilt of these anomalies with height is observed, suggesting that the preferred MCS genesis region is also characterized by strong baroclinity. The center of the negative anomaly, corresponding to the trough in the mean composite, is located upstream of the central United States with positive anomalies distributed on both sides. Negative (positive) geopotential height anomalies

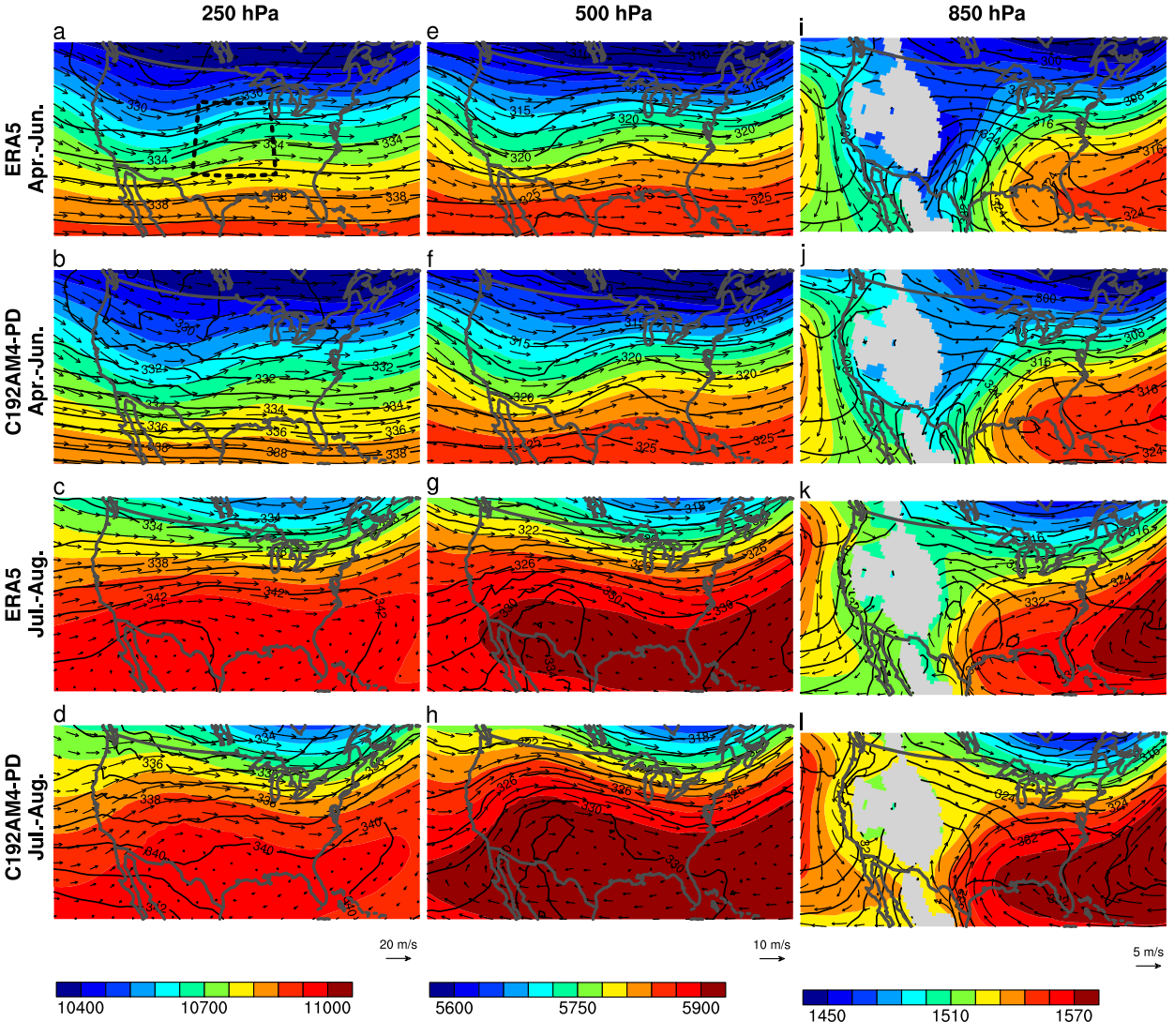

FIG. 14. Composites of mean geopotential height (shading; m), horizontal winds (vectors; m s^{-1}), and equivalent potential temperature (contours; K) at (a)–(d) 250, (e)–(h) 500, and (i)–(l) 850 hPa when MCSs are initiated over the central United States for 1985–2008 during spring and early summer in the first two rows and late summer in the bottom two rows based on ERA5 (first and third rows) and C192AM4-PD (second and fourth rows). Gray shading in (i)–(l) denotes regions with elevation higher than 1500 m.

are accompanied by anomalous cyclonic (anticyclonic) circulations, which jointly result in strong and northward penetrating flows. These southerly/southwesterly anomalies over the central United States coincide well with those above-normal θ_e anomalies. To put it together, when MCSs are initiated over the central United States, warmer and moister air has been advected from the Gulf of Mexico to the central United States by the intensified Great Plains low-level jet, which is then elevated by the strong ascending motion, moistening throughout the troposphere and creating favorable conditions for the MCS development. The model composites show a reasonable level of agreement with the observations (first row of Fig. 15). However, the negative geopotential anomalies in the model are smaller than those in the observations, while the positive anomalies are larger. Additionally, at 850 hPa, the distribution of geopotential anomalies is slightly distorted, with positive anomalies extending into Canada (second row of Fig. 15). During late summer, there is a shift northward in the alternating positive and negative geopotential height anomaly pattern. Positive anomalies are observed to the west of the U.S.–Canada border, while positive anomalies appear over the Great Lakes region. When combined with the mean state in Fig. 15, it becomes clear that the central United States is located ahead of a ridge. This is unfavorable for the development of MCSs as it suppresses upward motions. However, smaller-scale perturbations, such as midtropospheric shortwave forcing, may support the genesis of MCSs (Wang et al. 2009, 2011). In addition, like the cyclonic and anticyclonic pair, the low-level front is also located farther north compared to in spring and early summer (third row of Fig. 15). In contrast, the simulated geopotential height

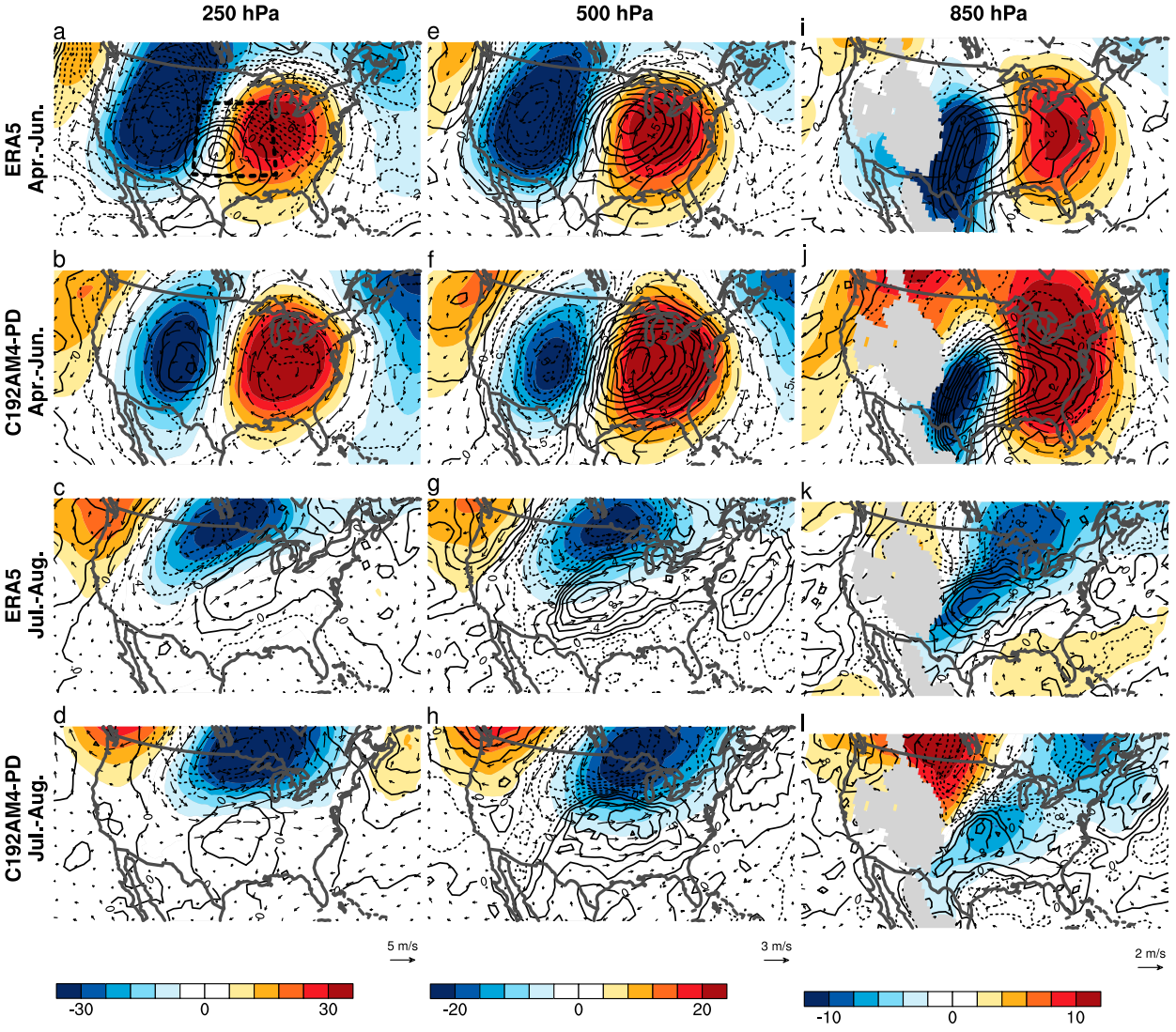

FIG. 15. As in Fig. 14, but for the corresponding anomaly fields. Anomalies are calculated as deviations from the corresponding time mean for each 3 h of the day and for each month at each grid point to remove the seasonal and diurnal variations.

anomaly patterns are shifted eastward compared to the observations. Additionally, the low-level patterns are largely distorted compared to mid- and upper-level patterns (fourth row of Fig. 15).

Building upon the fixed location composites, we show that the observed large-scale conditions favorable for MCS development are reasonably simulated by the model. We then use the storm-centered (sometimes called relative-location) composite (Lagrangian perspective) to determine the environmental features directly related to MCSs generated over the central United States. The storm-center composition is constructed using a moving latitude–longitude domain (5° × 5°). The center of the domain is located at the centroid of each MCS. The storm-centered composites of the wind, geopotential height, and θ_e anomalies are shown in Fig. 16 for both subperiods. The anomalous trough to the west of MCS is evident at all three levels during spring and early summer whereas the anomalous ridge to the east of MCS is less pronounced at 850 hPa within the 5° domain. Strong and northward extending tongues of anomalously higher-θ_e air are notable near the center of the MCSs. Compared to the upper levels, θ_e anomalies at lower levels (e.g., 850 hPa) are much larger and spread over a broader area, suggesting that the anomalous flow in the lower troposphere increases the potential instability. An anomalous cyclonic flow, located to the west of MCS centers, is observed at 850 hPa. This pattern is not visible at 500 hPa but is discernable at 700 hPa (figures not shown). Such a distribution can be seen in the typical MCS case as shown in Fig. 3, in which an anomalous cyclonic flow was present at 700 hPa trailing behind the stratiform region before the MCS reached its mature stage (1200 UTC), but it faded away as the MCS decayed afterward. This flow brings in relatively colder and drier air (lower θ_e) from west of the

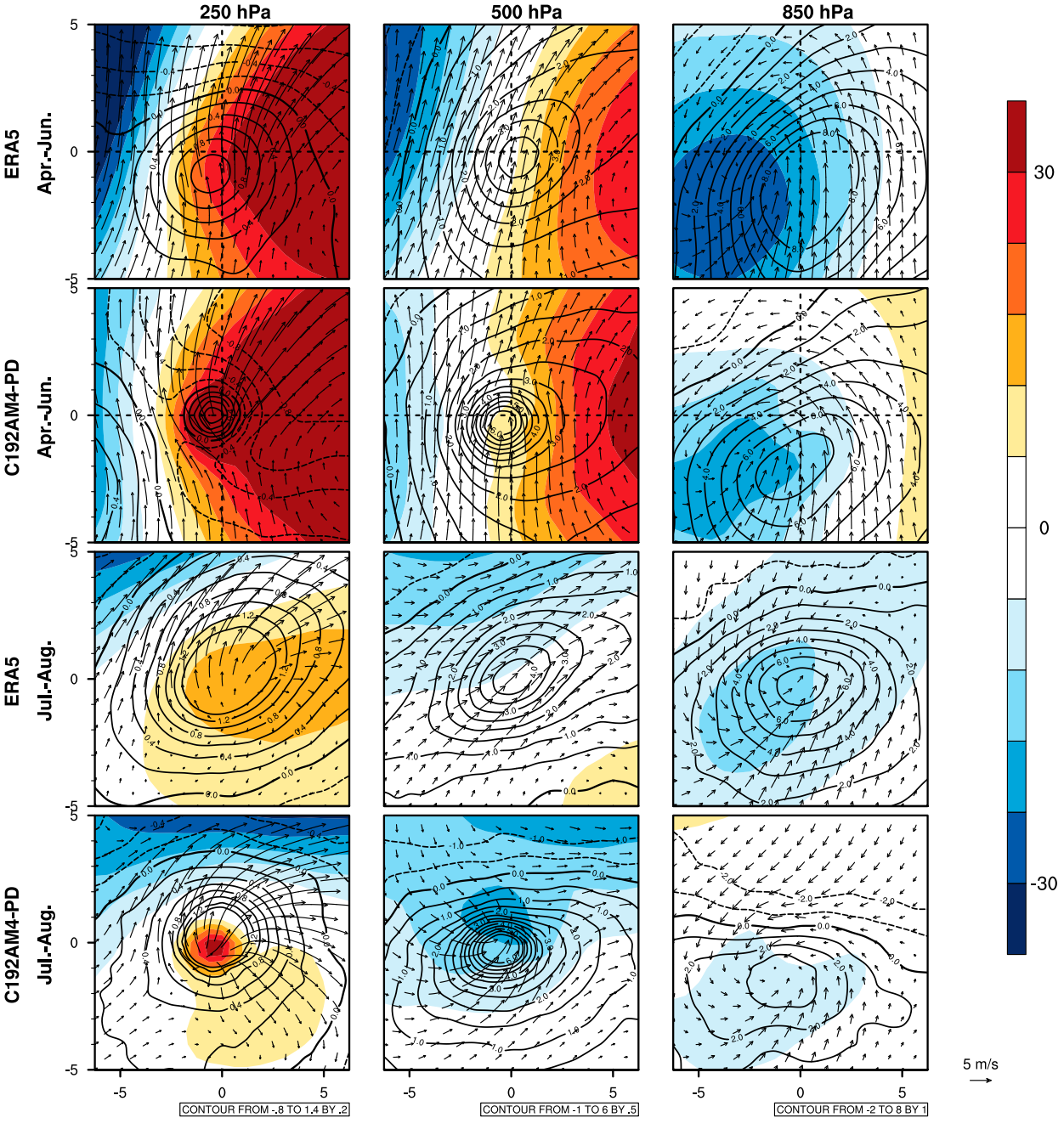

FIG. 16. Storm-centered composites anomalies of mean geopotential height (shading; m), horizontal winds (vectors; m s^{-1}), and equivalent potential temperature (contours; K) at (left) 250, (center) 500, and (right) 850 hPa for 1985–2008 during spring and early summer in the first two rows and late summer in the bottom two rows based on ERA5 (first and third rows) and C192AM4-PD (second and fourth rows).

composite domain, which is ingested into the rear-to-front sloping mesoscale downdraft that contributes to the cold pool propagation of the MCS (Houze 1989). At 250 hPa, a pronounced divergent signature emanating from the center of the MCS composites is observed. The simulated storm-centered composites reasonably reproduce the observed features, but the upper-level positive θ_e anomalies are concentrated near the composite center and the divergent flow is much stronger (second row in Fig. 16). The upper-level θ_e anomaly is usually related to the latent heat release when high cloud forms; the difference between the model and reanalysis may suggest that the parameterized convection or grid-scale ascent in the model is distorted. During late summer, the anomalies are weaker compared to those in spring and early summer, suggesting relatively weaker forcing for MCS initiation

during this period. This could also be attributed to the fact that the 5° domain may not be able to capture the entire large-scale environmental structures due to the northward shift. However, the upper-level θ_e anomaly biases observed in spring and early summer persist, which could be associated with the latent heating from the convection parameterization. Additionally, the circulation pattern and θ_e anomaly at the midlevel and low level are misrepresented in the model. This contrast suggests that summer convection could occur even with weak large-scale dynamical and thermodynamic perturbations, making MCSs inherently harder to simulate in summer. Thus, a more comprehensive understanding of these biases in different seasons is worthy of further investigation.

Results from these two types of composite analysis thus confirm that MCSs occurring during spring and early summer over the central United States usually form ahead of a trough embedded in the westerlies in combination with an enhanced Great Plains low-level moist jet from the Gulf of Mexico. The anomalous circulation associated with the development of MCSs, including divergent flows at upper levels and anomalous cyclonic flow at middle levels near the trailing portion of MCSs, further feed back onto the large-scale environment, helping sustain the trough and providing favorable conditions for upscale growth and maintenance of MCSs. All these processes are reasonably presented in the model. However, during late summer, these forcings become much weaker and the model fails to simulate the observed features.

e. *MCS-related precipitation*

A reasonable simulation of MCSs is the first step to better understanding changes in the warm season precipitation over the central United States given that MCSs are the more efficient rain producer of the two major rainfall types there (Hu et al. 2020). Significant increases in the warm season MCS-related precipitation have been observed during the past several decades mainly due to an increase in the occurrence frequency as well as the duration of MCSs (Feng et al. 2016; Hu et al. 2020). Such increases are projected to continue as the climate warms in the future (Prein et al. 2017). Similarly, we analyze the MCS-related precipitation in both the observation and model simulations during the two subperiods. It is worth pointing out that the MCS-related precipitation here only considers the centroid of each MCS since the intermediate shapefiles for each MCS are not saved out. Although the largest precipitation is usually found surrounding the centroid of MCS (Yang et al. 2017), this method excludes the large stratiform precipitation distributed in the trailing region of the convective line (one can see this clearly from Figs. 2 and 3). Thus, the results presented here may provide a lower limit of this estimation.

Figure 17 shows the total precipitation and the portion related to the MCSs for both subperiods. Compared to the total precipitation, the observed MCS-related precipitation is concentrated over the central United States and accounts for about 25% of the total precipitation during both subperiods, which is consistent with many other studies. However, the ratio of MCS-related precipitation to total precipitation is much lower than that reported (~60%) in Feng et al. (2021a), likely due to different calculation methods used in the studies. For the total precipitation, although the model generally captures the mean distribution (pattern correlation $R = 0.9$, $p < 0.001$) for both subperiods, it exhibits large dry biases over the central United States and southern coastal regions, with a wet bias over the eastern United States. The dry biases are more pronounced in late summer and have been found in many generations of GCMs (Klein et al. 2006; Mueller and Seneviratne 2014; Lin et al. 2017), which are argued to be accentuated by the difficulty in simulating MCSs in those coarser-resolution models (Feng et al. 2019; Lin et al. 2022). However, the simulated bias in MCS-related precipitation is less pronounced over the central United States in both subperiods, indicating that the non-MCS-related precipitation would be also biased low in the model simulations, and its deficit would be even larger than that of the MCS-related precipitation. Nonetheless, when averaged over the central United States, the simulated mean intensity of MCS-associated precipitation (6.9 mm day^{-1}) is larger than its observed counterpart (4.8 mm day^{-1}) during spring and early summer and is smaller (5.2 vs 5.4 mm day^{-1}) in late summer (Fig. 18). The simulated MCSs tend to generate light precipitation too frequently in spring and early summer, consistent with the drizzle syndrome as found in many GCMs (Dai 2006; Pendergrass and Hartmann 2014); meanwhile, they also produce more heavy precipitation (larger than 20 mm day^{-1}). Similar results have been found by Zhao (2022) that this model tends to overestimate the MCS-associated heavier precipitation and underestimate the associated weaker precipitation. While the simulated large precipitation events during late summer match the observations, the model underestimates the likelihood of light precipitation, leading to overall dry biases over the United States. Besides, we should be aware that these results may vary with the different partitioning and calculation of MCS and non-MCS associated precipitation; a closer investigation of this will be followed up in another study.

4. Discussion and conclusions

In summary, we evaluate the simulated MCS features over the United States from the newly developed GFDL global high-resolution (~50 km) model (C192AM4) by comparing them with the observations during the warm season, which is further divided into two subperiods: spring to early summer (April–June) and late summer (July–August). Our analysis focuses on the central United States to facilitate comparison with previous studies, most of which have also focused on this region (Feng et al. 2021a). Our results show that the spatial distribution of occurrence and genesis frequency of MCSs is well simulated over the central United States in both subperiods. Additionally, the seasonality of MCS occurrence and genesis frequency is well reproduced by the model when averaged over the central United States, which is consistent with observations showing frequent MCS activity during the warm season. The model reliably reproduces the mean spatial distribution and the probability distribution of MCS duration, MCS-associated T_b values, translation speed, size, and duration–size relationship over the central United States. Furthermore, the

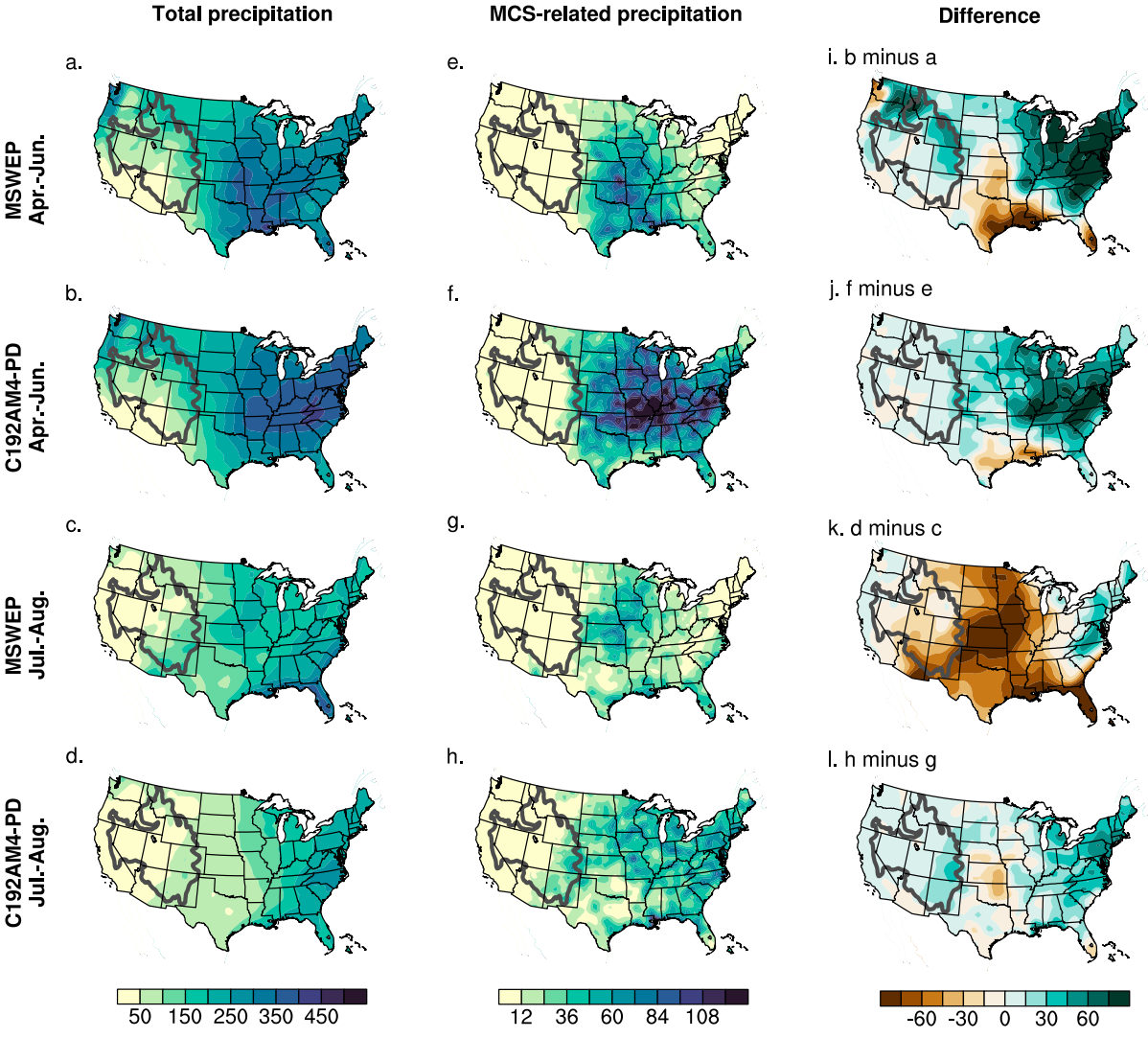

FIG. 17. (left) Total precipitation (mm) and (center) MCS-related precipitation (mm) for 1985–2008 during (a),(b),(e),(f) spring and early summer and (c),(d),(g),(h) late summer based on MSWEP (first and third rows) and C192AM4-PD (second and fourth rows). (i)–(l) Differences are shown: (i) is (b) minus (a), (j) is (f) minus (e), (k) is (d) minus (c), and (l) is (h) minus (g). The thick gray contour in (a)–(f) denotes the 1500-m isoline.

model captures the favorable large-scale circulation pattern associated with MCS development over the central United States during spring and early summer, where MCSs usually form ahead of a trough embedded in the westerlies. Moisture needed for the development of MCS is advected by the enhanced GPLLJ from the Gulf of Mexico. When MCSs are initiated, they feed back on the large-scale circulation pattern by generating divergent flows at upper levels and cyclonic anomalies at middle levels near the trailing portion of MCSs. These anomalous circulations further help sustain the trough and provide favorable conditions for the upscale growth and maintenance of MCSs.

However, the model misrepresents the amplitude and the phase of the diurnal cycle of MCS during both subperiods. The amplitude of the diurnal cycle is systematically weaker over the central United States. Also, the simulated MCSs prefer to form in early morning hours rather than the observed late afternoon to evening hours. Moreover, the spatial distribution of occurrence and genesis frequency of MCSs over the eastern United States is substantially overestimated, with larger biases seen in early spring and summer. Additionally, while large-scale circulation patterns are reasonably represented in spring and early summer, they are poorly simulated in the model during summer. While the model overestimates MCS-related precipitation during spring and early summer, this bias alone cannot account for the large dry bias observed in total precipitation over the central U.S. However, the dry biases associated with MCSs during late summer likely contribute to the overall precipitation deficit.

Overall, our analysis suggest C192AM4 model is skillful at simulating some of the observed characteristics of MCSs over

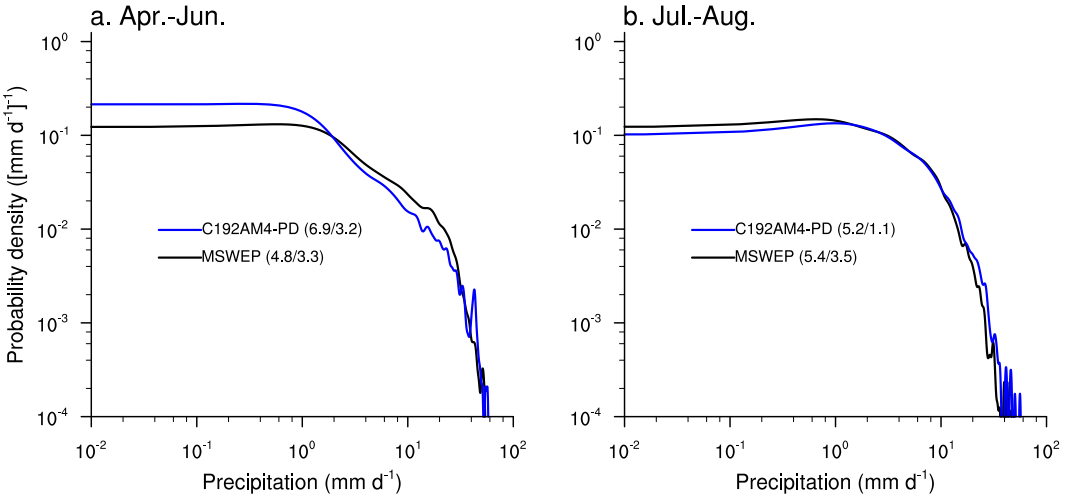

FIG. 18. Observed (MSWEP; black) and simulated (C192AM4-PD; blue) probability density distribution of MCS-related precipitation for 1985–2008 during (a) spring and early summer and (b) late summer. The respective mean/medium values are listed.

the central United States, making it a potentially useful tool to study the interaction between MCSs and the large-scale circulation, changes in MCS-related weather extremes, and the response of MCS to global warming. But much remains to be done, especially for the weak and wrong diurnal cycle of MCSs and the large biases in the occurrence and genesis frequency of MCSs over the eastern United States. We are currently evaluating the performance of a 25-km model with the hope of seeing improvements in resolved synoptic-scale progresses. For future works, sensitivity tests will be conducted to differentiate the impact of physical processes from the large-scale environments on the simulated MCS development. Furthermore, it may be a minor concern, but the conversion from OLR to T_b could also introduce some uncertainties. Finally, the detection of MCS in this study is merely based on T_b from geostationary satellite observations. Lacking information on the internal structure of convection, one risk of this method would be that the identified MCS can be confused with cirrus or stratiform cloud that are not necessarily formed from these convective systems. Cold cloud systems could also be generated from extratropical cyclones and frontal systems over midlatitudes. A few studies, by combining both the satellite T_b and the ground radar that provides three-dimensional convective/stratiform features, have found to be more accurate to illustrate the evolution of MCSs over the United States (e.g., Feng et al. 2019). But these radar datasets are only available for a certain period and radar reflectivity is not a standard variable in the model. Recently, one feasible way to reduce misclassification of MCSs attributable to cirrus cloud layers has been developed by Feng et al. (2021b) and Zhao (2022). This method includes surface precipitation as another feature to characterize MCSs. By comparison with available ground-based radar, they showed that MCSs detected by the new methodology are comparable to those observed by radar networks. The more accessible precipitation dataset enables us to apply this new method to the model simulations, which will be analyzed in a follow-up study.

Acknowledgments. The authors thank Leo J. Donner and Zhihong Tan for useful discussion and commenting on earlier versions of this paper, and three anonymous reviewers for their comments on this manuscript. This research from the Geophysical Fluid Dynamics Laboratory is supported by NOAA's Science Collaboration Program and administered by UCAR's Cooperative Programs for the Advancement of Earth System Science (CPAESS) under Awards NA16NWS4620043 and NA18NWS4620043B.

Data availability statement. The brightness temperature datasets from the Cloud Archive User Service (CLAUS) product are available at https://data.ceda.ac.uk/badc/claus/data/. The Multi-Source Weighted-Ensemble Precipitation, version 2 (MSWEP V2) precipitation data can be found at https://gloh2o.org/mswep/. Mosaics of NEXRAD base reflectivity are generated and archived by the Iowa Environmental Mesonet, which can be found at https://mesonet.agron.iastate.edu/docs/nexrad_mosaic/. The C192AM4 model outputs can be downloaded from https://esgf-node.llnl.gov/search/cmip6/. The GFDL AM4 model source code can be obtained from https://data1.gfdl.noaa.gov/nomads/forms/am4.0/.

REFERENCES

Alexander, M. J., and T. J. Dunkerton, 1999: A spectral parameterization of mean-flow forcing due to breaking gravity waves. *J. Atmos. Sci.*, **56**, 4167–4182, https://doi.org/10.1175/1520-0469(1999)056<4167:ASPOMF>2.0.CO;2.

Anderson, C. J., and R. W. Arritt, 2001: Mesoscale convective systems over the United States during the 1997–98 El Niño. *Mon. Wea. Rev.*, **129**, 2443–2457, https://doi.org/10.1175/1520-0493(2001)129<2443:MCSOTU>2.0.CO;2.

Balling, R. C., Jr., 1985: Warm season nocturnal precipitation in the Great Plains of the United States. *J. Climate Appl. Meteor.*, **24**, 1383–1387, https://doi.org/10.1175/1520-0450(1985)024<1383:WSNPIT>2.0.CO;2.

Beck, H. E., E. F. Wood, M. Pan, C. K. Fisher, D. G. Miralles, A. I. J. M. van Dijk, T. R. McVicar, and R. F. Adler, 2019: MSWEP V2 global 3-hourly 0.1° precipitation: Methodology and quantitative assessment. *Bull. Amer. Meteor. Soc.*, **100**, 473–500, https://doi.org/10.1175/BAMS-D-17-0138.1.

Carbone, R. E., and J. D. Tuttle, 2008: Rainfall occurrence in the U.S. warm season: The diurnal cycle. *J. Climate*, **21**, 4132–4146, https://doi.org/10.1175/2008JCLI2275.1.

Cheeks, S. M., S. Fueglistaler, and S. T. Garner, 2020: A satellite-based climatology of central and southeastern US mesoscale convective systems. *Mon. Wea. Rev.*, **148**, 2607–2621, https://doi.org/10.1175/MWR-D-20-0027.1.

Chen, C.-C., J. Richter, C. Liu, M. W. Moncrieff, Q. Tang, W. Lin, S. Xie, and P. J. Rasch, 2021: Effects of organized convection parameterization on the MJO and precipitation in E3SMv1. Part I: Mesoscale heating. *J. Adv. Model. Earth Syst.*, **13**, e2020MS002401, https://doi.org/10.1029/2020MS002401.

Clark, A. J., W. A. Gallus Jr., and T.-C. Chen, 2007: Comparison of the diurnal precipitation cycle in convection-resolving and non-convection-resolving mesoscale models. *Mon. Wea. Rev.*, **135**, 3456–3473, https://doi.org/10.1175/MWR3467.1.

Coniglio, M. C., J. Y. Hwang, and D. J. Stensrud, 2010: Environmental factors in the upscale growth and longevity of MCSs derived from rapid update cycle analyses. *Mon. Wea. Rev.*, **138**, 3514–3539, https://doi.org/10.1175/2010MWR3233.1.

Corfidi, S. F., 2003: Cold pools and MCS propagation: Forecasting the motion of downwind-developing MCSs. *Wea. Forecasting*, **18**, 997–1017, https://doi.org/10.1175/1520-0434(2003)018<0997:CPAMPF>2.0.CO;2.

Dai, A., 2006: Precipitation characteristics in eighteen coupled climate models. *J. Climate*, **19**, 4605–4630, https://doi.org/10.1175/JCLI3884.1.

Davis, C. A., K. W. Manning, R. E. Carbone, S. B. Trier, and J. D. Tuttle, 2003: Coherence of warm-season continental rainfall in numerical weather prediction models. *Mon. Wea. Rev.*, **131**, 2667–2679, https://doi.org/10.1175/1520-0493(2003)131<2667:COWCRI>2.0.CO;2.

Dong, W., M. Zhao, Y. Ming, and V. Ramaswamy, 2021: Representation of tropical mesoscale convective systems in a general circulation model: Climatology and response to global warming. *J. Climate*, **34**, 5657–5671, https://doi.org/10.1175/JCLI-D-20-0535.1.

——, ——, ——, and ——, 2022: Significant increase in sea surface temperature at the genesis of tropical mesoscale convective systems. *Geophys. Res. Lett.*, **49**, e2022GL101950, https://doi.org/10.1029/2022GL101950.

——, Y. L. Lin, M. H. Zhang, and X. M. Huang, 2020: Footprint of tropical mesoscale convective system variability on stratospheric water vapor. *Geophys. Res. Lett.*, **47**, e2019GL086320, https://doi.org/10.1029/2019GL086320.

Donner, L. J., 1993: A cumulus parameterization including mass fluxes, vertical momentum dynamics, and mesoscale effects. *J. Atmos. Sci.*, **50**, 889–906, https://doi.org/10.1175/1520-0469(1993)050<0889:ACPIMF>2.0.CO;2.

——, C. J. Seman, R. S. Hemler, and S. Fan, 2001: A cumulus parameterization including mass fluxes, convective vertical velocities, and mesoscale effects: Thermodynamic and hydrological aspects in a general circulation model. *J. Climate*, **14**, 3444–3463, https://doi.org/10.1175/1520-0442(2001)014<3444:ACPIMF>2.0.CO;2.

Feng, Z., L. R. Leung, S. Hagos, R. A. Houze, C. D. Burleyson, and K. Balaguru, 2016: More frequent intense and long-lived storms dominate the springtime trend in central US rainfall. *Nat. Commun.*, **7**, 13429, https://doi.org/10.1038/ncomms13429.

——, ——, R. A. Houze Jr., S. Hagos, J. Hardin, Q. Yang, B. Han, and J. Fan, 2018: Structure and evolution of mesoscale convective systems: Sensitivity to cloud microphysics in convection-permitting simulations over the United States. *J. Adv. Model. Earth Syst.*, **10**, 1470–1494, https://doi.org/10.1029/2018MS001305.

——, R. A. Houze Jr., L. R. Leung, F. Song, J. C. Hardin, J. Wang, W. I. Gustafson Jr., and C. R. Homeyer, 2019: Spatiotemporal characteristics and large-scale environments of mesoscale convective systems east of the Rocky Mountains. *J. Climate*, **32**, 7303–7328, https://doi.org/10.1175/JCLI-D-19-0137.1.

——, F. Song, K. Sakaguchi, and L. R. Leung, 2021a: Evaluation of mesoscale convective systems in climate simulations: Methodological development and results from MPAS-CAM over the United States. *J. Climate*, **34**, 2611–2633, https://doi.org/10.1175/JCLI-D-20-0136.1.

——, and Coauthors, 2021b: A global high-resolution mesoscale convective system database using satellite-derived cloud tops, surface precipitation, and tracking. *J. Geophys. Res. Atmos.*, **126**, e2020JD034202, https://doi.org/10.1029/2020JD034202.

Fritsch, J. M., R. J. Kane, and C. R. Chelius, 1986: The contribution of mesoscale convective weather systems to the warm-season precipitation in the United-States. *J. Climate Appl. Meteor.*, **25**, 1333–1345, https://doi.org/10.1175/1520-0450(1986)025<1333:TCOMCW>2.0.CO;2.

Garner, S. T., 2005: A topographic drag closure built on an analytical base flux. *J. Atmos. Sci.*, **62**, 2302–2315, https://doi.org/10.1175/JAS3496.1.

——, 2018: Ground-truth model evaluation of subgrid orographic base-flux parameterization. *J. Atmos. Sci.*, **75**, 3653–3670, https://doi.org/10.1175/JAS-D-17-0368.1.

Gettelman, A., P. Callaghan, V. E. Larson, C. M. Zarzycki, J. T. Bacmeister, P. H. Lauritzen, P. A. Bogenschutz, and R. B. Neale, 2018: Regional climate simulations with the Community Earth System Model. *J. Adv. Model. Earth Syst.*, **10**, 1245–1265, https://doi.org/10.1002/2017MS001227.

Golaz, J.-C., and Coauthors, 2019: The DOE E3SM coupled model version 1: Overview and evaluation at standard resolution. *J. Adv. Model. Earth Syst.*, **11**, 2089–2129, https://doi.org/10.1029/2018MS001603.

Grabowski, W. W., and P. K. Smolarkiewicz, 1999: CRCP: A cloud resolving convection parameterization for modeling the tropical convecting atmosphere. *Physica D*, **133**, 171–178, https://doi.org/10.1016/S0167-2789(99)00104-9.

Haarsma, R. J., and Coauthors, 2016: High Resolution Model Intercomparison Project (HighResMIP v1.0) for CMIP6. *Geosci. Model Dev.*, **9**, 4185–4208, https://doi.org/10.5194/gmd-9-4185-2016.

Hartmann, D. L., H. H. Hendon, and R. A. Houze Jr., 1984: Some implications of the mesoscale circulations in tropical cloud clusters for large-scale dynamics and climate. *J. Atmos. Sci.*, **41**, 113–121, https://doi.org/10.1175/1520-0469(1984)041<0113:SIOTMC>2.0.CO;2.

Hersbach, H., and Coauthors, 2020: The ERA5 global reanalysis. *Quart. J. Roy. Meteor. Soc.*, **146**, 1999–2049, https://doi.org/10.1002/qj.3803.

Hoch, J., and P. Markowski, 2005: A climatology of springtime dryline position in the US Great Plains region. *J. Climate*, **18**, 2132–2137, https://doi.org/10.1175/JCLI3392.1.

Hodges, K. I., D. W. Chappell, G. J. Robinson, and G. Yang, 2000: An improved algorithm for generating global window brightness temperatures from multiple satellite infrared imagery. *J. Atmos. Oceanic Technol.*, **17**, 1296–1312, https://doi.org/10.1175/1520-0426(2000)017<1296:AIAFGG>2.0.CO;2.

Houze, R. A., Jr., 1989: Observed structure of mesoscale convective systems and implications for large-scale heating. *Quart. J. Roy. Meteor. Soc.*, **115**, 425–461, https://doi.org/10.1002/qj.49711548702.

——, 2004: Mesoscale convective systems. *Rev. Geophys.*, **42**, RG4003, https://doi.org/10.1029/2004RG000150.

——, 2018: 100 years of research on mesoscale convective systems. *A Century of Progress in Atmospheric and Related Sciences: Celebrating the American Meteorological Society Centennial*, *Meteor. Monogr.*, No. 59, Amer. Meteor. Soc., https://doi.org/10.1175/AMSMONOGRAPHS-D-19-0006.1.

——, B. F. Smull, and P. Dodge, 1990: Mesoscale organization of springtime rainstorms in Oklahoma. *Mon. Wea. Rev.*, **118**, 613–654, https://doi.org/10.1175/1520-0493(1990)118<0613:MOOSRI>2.0.CO;2.

——, K. L. Rasmussen, M. D. Zuluaga, and S. R. Brodzik, 2015: The variable nature of convection in the tropics and subtropics: A legacy of 16 years of the tropical rainfall measuring mission satellite. *Rev. Geophys.*, **53**, 994–1021, https://doi.org/10.1002/2015RG000488.

Hu, H., L. R. Leung, and Z. Feng, 2020: Observed warm-season characteristics of MCS and non-MCS rainfall and their recent changes in the central United States. *Geophys. Res. Lett.*, **47**, e2019GL086783, https://doi.org/10.1029/2019GL086783.

Huang, X., C. Hu, X. Huang, Y. Chu, Y.-h. Tseng, G. J. Zhang, and Y. Lin, 2018: A long-term tropical mesoscale convective systems dataset based on a novel objective automatic tracking algorithm. *Climate Dyn.*, **51**, 3145–3159, https://doi.org/10.1007/s00382-018-4071-0.

Jakob, C., and S. A. Klein, 2000: A parameterization of the effects of cloud and precipitation overlap for use in general circulation models. *Quart. J. Roy. Meteor. Soc.*, **126**, 2525–2544, https://doi.org/10.1002/qj.49712656809.

Junker, N. W., R. S. Schneider, and S. L. Fauver, 1999: A study of heavy rainfall events during the great Midwest flood of 1993. *Wea. Forecasting*, **14**, 701–712, https://doi.org/10.1175/1520-0434(1999)014<0701:ASOHRE>2.0.CO;2.

Klein, S. A., X. Jiang, J. Boyle, S. Malyshev, and S. Xie, 2006: Diagnosis of the summertime warm and dry bias over the U.S. southern Great Plains in the GFDL climate model using a weather forecasting approach. *Geophys. Res. Lett.*, **33**, L18805, https://doi.org/10.1029/2006GL027567.

Laing, A. G., and J. M. Fritsch, 1997: The global population of mesoscale convective complexes. *Quart. J. Roy. Meteor. Soc.*, **123**, 389–405, https://doi.org/10.1002/qj.49712353807.

——, and ——, 2000: The large-scale environments of the global populations of mesoscale convective complexes. *Mon. Wea. Rev.*, **128**, 2756–2776, https://doi.org/10.1175/1520-0493(2000)128<2756:TLSEOT>2.0.CO;2.

Lin, G., J. Fan, Z. Feng, W. I. Gustafson Jr., P.-L. Ma, and K. Zhang, 2019: Can the multiscale modeling framework (MMF) simulate the MCS-associated precipitation over the Central United States? *J. Adv. Model. Earth Syst.*, **11**, 4669–4686, https://doi.org/10.1029/2019MS001849.

——, C. R. Jones, L. R. Leung, Z. Feng, and M. Ovchinnikov, 2022: Mesoscale convective systems in a superparameterized E3SM simulation at high resolution. *J. Adv. Model. Earth Syst.*, **14**, e2021MS002660, https://doi.org/10.1029/2021MS002660.

Lin, Y., W. Dong, M. Zhang, Y. Xie, W. Xue, J. Huang, and Y. Luo, 2017: Causes of model dry and warm bias over central US and impact on climate projections. *Nat. Commun.*, **8**, 881, https://doi.org/10.1038/s41467-017-01040-2.

Lock, A. P., A. R. Brown, M. R. Bush, G. M. Martin, and R. N. B. Smith, 2000: A new boundary layer mixing scheme. Part I: Scheme description and single-column model tests. *Mon. Wea. Rev.*, **128**, 3187–3199, https://doi.org/10.1175/1520-0493(2000)128<3187:ANBLMS>2.0.CO;2.

Machado, L. A. T., W. B. Rossow, R. L. Guedes, and A. W. Walker, 1998: Life cycle variations of mesoscale convective systems over the Americas. *Mon. Wea. Rev.*, **126**, 1630–1654, https://doi.org/10.1175/1520-0493(1998)126<1630:LCVOMC>2.0.CO;2.

Maddox, R. A., 1980: Mesoscale convective complexes. *Bull. Amer. Meteor. Soc.*, **61**, 1374–1387, https://doi.org/10.1175/1520-0477(1980)061<1374:MCC>2.0.CO;2.

——, 1983: Large-scale meteorological conditions associated with midlatitude, mesoscale convective complexes. *Mon. Wea. Rev.*, **111**, 1475–1493, https://doi.org/10.1175/1520-0493(1983)111<1475:LSMCAW>2.0.CO;2.

Mapes, B. E., and R. A. Houze Jr., 1993: Cloud clusters and superclusters over the oceanic warm pool. *Mon. Wea. Rev.*, **121**, 1398–1416, https://doi.org/10.1175/1520-0493(1993)121<1398:CCASOT>2.0.CO;2.

——, S. Tulich, J. Lin, and P. Zuidema, 2006: The mesoscale convection life cycle: Building block or prototype for large-scale tropical waves? *Dyn. Atmos. Oceans*, **42**, 3–29, https://doi.org/10.1016/j.dynatmoce.2006.03.003.

Mitchell, T., and D. M. Schultz, 2020: A synoptic climatology of spring dryline convection in the southern Great Plains. *Wea. Forecasting*, **35**, 1561–1582, https://doi.org/10.1175/WAF-D-19-0160.1.

Moncrieff, M. W., 2004: Analytic representation of the large-scale organization of tropical convection. *J. Atmos. Sci.*, **61**, 1521–1538, https://doi.org/10.1175/1520-0469(2004)061<1521:AROTLO>2.0.CO;2.

——, 2010: The multiscale organization of moist convection and the intersection of weather and climate. *Climate Dynamics: Why Does Climate Vary? Geophys. Monogr.*, **189**, 3–26, https://doi.org/10.1029/2008GM000838.

——, 2019: Toward a dynamical foundation for organized convection parameterization in GCMs. *Geophys. Res. Lett.*, **46**, 14 103–14 108, https://doi.org/10.1029/2019GL085316.

——, and C. Liu, 2006: Representing convective organization in prediction models by a hybrid strategy. *J. Atmos. Sci.*, **63**, 3404–3420, https://doi.org/10.1175/JAS3812.1.

——, D. E. Waliser, M. J. Miller, M. A. Shapiro, G. R. Asrar, and J. Caughey, 2012: Multiscale convective organization and the YOTC virtual global field campaign. *Bull. Amer. Meteor. Soc.*, **93**, 1171–1187, https://doi.org/10.1175/BAMS-D-11-00233.1.

——, C. Liu, and P. Bogenschutz, 2017: Simulation, modeling, and dynamically based parameterization of organized tropical convection for global climate models. *J. Atmos. Sci.*, **74**, 1363–1380, https://doi.org/10.1175/JAS-D-16-0166.1.

Mueller, B., and S. I. Seneviratne, 2014: Systematic land climate and evapotranspiration biases in CMIP5 simulations. *Geophys. Res. Lett.*, **41**, 128–134, https://doi.org/10.1002/2013GL058055.

Nesbitt, S. W., R. Cifelli, and S. A. Rutledge, 2006: Storm morphology and rainfall characteristics of TRMM precipitation

features. *Mon. Wea. Rev.*, **134**, 2702–2721, https://doi.org/10.1175/MWR3200.1.

Nguyen, H., and J.-P. Duvel, 2008: Synoptic wave perturbations and convective systems over equatorial Africa. *J. Climate*, **21**, 6372–6388, https://doi.org/10.1175/2008JCLI2409.1.

Paynter, D., and V. Ramaswamy, 2012: Variations in water vapor continuum radiative transfer with atmospheric conditions. *J. Geophys. Res.*, **117**, D16310, https://doi.org/10.1029/2012JD017504.

——, and ——, 2014: Investigating the impact of the shortwave water vapor continuum upon climate simulations using GFDL global models. *J. Geophys. Res. Atmos.*, **119**, 10 720–10 737, https://doi.org/10.1002/2014JD021881.

Pendergrass, A. G., and D. L. Hartmann, 2014: Changes in the distribution of rain frequency and intensity in response to global warming. *J. Climate*, **27**, 8372–8383, https://doi.org/10.1175/JCLI-D-14-00183.1.

Peters, J. M., and R. S. Schumacher, 2015: Mechanisms for organization and echo training in a flash-flood-producing mesoscale convective system. *Mon. Wea. Rev.*, **143**, 1058–1085, https://doi.org/10.1175/MWR-D-14-00070.1.

Prein, A. F., C. Liu, K. Ikeda, S. B. Trier, R. M. Rasmussen, G. J. Holland, and M. P. Clark, 2017: Increased rainfall volume from future convective storms in the US. *Nat. Climate Change*, **7**, 880–884, https://doi.org/10.1038/s41558-017-0007-7.

——, ——, ——, R. Bullock, R. M. Rasmussen, G. J. Holland, and M. Clark, 2020: Simulating North American mesoscale convective systems with a convection-permitting climate model. *Climate Dyn.*, **55**, 95–110, https://doi.org/10.1007/s00382-017-3993-2.

Roca, R., J. Aublanc, P. Chambon, T. Fiolleau, and N. Viltard, 2014: Robust observational quantification of the contribution of mesoscale convective systems to rainfall in the tropics. *J. Climate*, **27**, 4952–4958, https://doi.org/10.1175/JCLI-D-13-00628.1.

Rotstayn, L. D., 1997: A physically based scheme for the treatment of stratiform clouds and precipitation in large-scale models. I, Description and evaluation of the microphysical processes. *Quart. J. Roy. Meteor. Soc.*, **123**, 1227–1282, https://doi.org/10.1002/qj.49712354106.

Schumacher, R. S., and R. H. Johnson, 2006: Characteristics of us extreme rain events during 1999–2003. *Wea. Forecasting*, **21**, 69–85, https://doi.org/10.1175/WAF900.1.

Schwarzkopf, D. M., and S. B. Fels, 1991: The simplified exchange method revisited: An accurate, rapid method for computation of infrared cooling rates and fluxes. *J. Geophys. Res.*, **96**, 9075–9096, https://doi.org/10.1029/89JD01598.

Song, F., Z. Feng, L. R. Leung, R. A. Houze Jr., J. Wang, J. Hardin, and C. R. Homeyer, 2019: Contrasting spring and summer large-scale environments associated with mesoscale convective systems over the U.S. Great Plains. *J. Climate*, **32**, 6749–6767, https://doi.org/10.1175/JCLI-D-18-0839.1.

Tao, W.-K., and J.-D. Chern, 2017: The impact of simulated mesoscale convective systems on global precipitation: A multiscale modeling study. *J. Adv. Model. Earth Syst.*, **9**, 790–809, https://doi.org/10.1002/2016MS000836.

Trier, S. B., and D. B. Parsons, 1993: Evolution of environmental conditions preceding the development of a nocturnal mesoscale convective complex. *Mon. Wea. Rev.*, **121**, 1078–1098, https://doi.org/10.1175/1520-0493(1993)121<1078:EOECPT>2.0.CO;2.

Virts, K. S., and R. A. Houze Jr., 2015: Clouds and water vapor in the tropical tropopause transition layer over mesoscale convective systems. *J. Atmos. Sci.*, **72**, 4739–4753, https://doi.org/10.1175/JAS-D-15-0122.1.

Wang, S.-Y., T.-C. Chen, and S. E. Taylor, 2009: Evaluations of NAM forecasts on midtropospheric perturbation-induced convective storms over the U.S. northern plains. *Wea. Forecasting*, **24**, 1309–1333, https://doi.org/10.1175/2009WAF2222185.1.

——, ——, and E. S. Takle, 2011: Climatology of summer midtropospheric perturbations in the US northern plains. Part II: Large-scale effects of the Rocky Mountains on genesis. *Climate Dyn.*, **36**, 1221–1237, https://doi.org/10.1007/s00382-010-0765-7.

Xie, S., L.-Y. Leung, Z. Feng, W. Lin, C.-C. Chen, J. Richter, and J. Fan, 2020: Fy2020 fourth quarter performance metric: Evaluate improvement in simulations of mesoscale convective systems from new parameterization developments in E3SM. Tech. Rep. LLNL-TR-814618, 13 pp., https://doi.org/10.2172/1661028.

Yang, Q., R. A. Houze Jr., L. R. Leung, and Z. Feng, 2017: Environments of long-lived mesoscale convective systems over the central United States in convection permitting climate simulations. *J. Geophys. Res. Atmos.*, **122**, 13 288–13 307, https://doi.org/10.1002/2017JD027033.

——, A. J. Majda, and M. W. Moncrieff, 2019: Upscale impact of mesoscale convective systems and its parameterization in an idealized GCM for an MJO analog above the equator. *J. Atmos. Sci.*, **76**, 865–892, https://doi.org/10.1175/JAS-D-18-0260.1.

Yuan, J., and R. A. Houze Jr., 2010: Global variability of mesoscale convective system anvil structure from A-Train satellite data. *J. Climate*, **23**, 5864–5888, https://doi.org/10.1175/2010JCLI3671.1.

Zhao, M., 2020: Simulations of atmospheric rivers, their variability, and response to global warming using GFDL's new high-resolution general circulation model. *J. Climate*, **33**, 10 287–10 303, https://doi.org/10.1175/JCLI-D-20-0241.1.

——, 2022: A study of AR-, TS-, and MCS-associated precipitation and extreme precipitation in present and warmer climates. *J. Climate*, **35**, 479–497, https://doi.org/10.1175/JCLI-D-21-0145.1.

——, I. M. Held, S.-J. Lin, and G. A. Vecchi, 2009: Simulations of global hurricane climatology, interannual variability, and response to global warming using a 50-km resolution GCM. *J. Climate*, **22**, 6653–6678, https://doi.org/10.1175/2009JCLI3049.1.

——, and Coauthors, 2016: Uncertainty in model climate sensitivity traced to representations of cumulus precipitation microphysics. *J. Climate*, **29**, 543–560, https://doi.org/10.1175/JCLI-D-15-0191.1.

——, and Coauthors, 2018a: The GFDL global atmosphere and land model AM4.0/LM4.0: 1. Simulation characteristics with prescribed SSTs. *J. Adv. Model. Earth Syst.*, **10**, 691–734, https://doi.org/10.1002/2017MS001208.

——, and Coauthors, 2018b: The GFDL global atmosphere and land model AM4.0/LM4.0: 2. Model description, sensitivity studies, and tuning strategies. *J. Adv. Model. Earth Syst.*, **10**, 735–769, https://doi.org/10.1002/2017MS001209.